High-altitude atmospheric turbulence and infrasound measurements using a balloon-launched small uncrewed aircraft system

Anisa N. Haghighi[1], Ryan D. Nolin[1], Gary D. Pundsack[2], Nick Craine[2], Aliaksei Stratsilatau[3], and Sean C. C. Bailey[1]

[1]Department of Mechanical and Aerospace Engineering, University of Kentucky, Lexington, Kentucky 40506, USA
[2]Stratodynamics Inc., 16192 Coastal Highway, Lewes, Delaware 19958, USA
[3]UAVOS Inc., 541 Jefferson Ave, Ste 100, Redwood City, California 94063, USA

Correspondence: Sean Bailey (sean.bailey@uky.edu)

Abstract. This study investigates the use of a balloon-launched small Uncrewed Aircraft System (sUAS) for the measurement of turbulence in the troposphere and lower stratosphere. The sUAS was a glider which could conduct an automated descent following a designated flight trajectory and was equipped with in-situ sensors for measuring thermodynamic and kinematic atmospheric properties typically measured using balloon-borne instruments. By being able to transect the air, the glider allows for turbulence wavelengths to be sampled at a particular altitude, improving statistical convergence and spatial resolution of derived statistics from its in-situ sensors. In addition, this aircraft was equipped with an infrasonic microphone to assess its suitability for the remote detection of clear-air turbulence. The capabilities of the sUAS and sensing systems were tested using three flights conducted in 2021 in New Mexico, U.S.A.. It was found that the profiles of temperature, humidity and horizontal winds measured during descent were in broad agreement with those made by radiosonde data published by the U.S. National Weather Service, although these measurements were separated by up to 380 km spatially and by 3 to 5 hours temporally. Importantly, analysis of the statistics produced along the flight trajectory allowed the identification of key turbulence quantities and features which allowed the connection to be made between the locations of increased turbulence intensity and the source of its generation. In addition, the infrasonic microphone sound amplitude was found to increase in regions of where increased turbulence intensity was observed, suggesting that the microphone was sensing turbulence. However, interpretation of the microphone signal was convoluted by the altitude dependence of the microphone response and the difficulty in discriminating individual sources from within the microphone signal.

1 Introduction

Due to its importance in weather and climate, the formation and evolution of atmospheric turbulence has long been of scientific interest. In addition, the presence of atmospheric turbulence also poses an aviation hazard that is challenging to predict and

detect. This latter point is particularly true for high-altitude autonomous flight, a regime which is being increasingly pursued in the form of High-Altitude Pseudo-Satellite, or High-Altitude Platform Station, (HAPS) aircraft, which can provide communication and remote observation capabilities at relatively low cost (Gonzalo et al., 2018; D'Oliveira et al., 2016; Hasan et al., 2022). By the nature of the flight conditions under which these aircraft operate, they tend to be structurally fragile with narrow

25 performance envelopes for which controlled flight can be maintained.

Despite the higher stability of the stratosphere, turbulence can still occur in this cloudless atmospheric layer due to shear instabilities and gravity wave breaking and such features are often referred to as clear air turbulence There are several potential sources of clear air turbulence. For example, the geospatial instability caused by the horizontal movement of air above terrain (e.g. mountains) can result in upward vertical motions (Cunningham and Keyser, 2015), wind shear and ultimately turbulence

30 production within their proximity. Another source of clear air turbulence is the presence of a jet stream. Jet streams generally occur at the tropopause (the boundary region between the troposphere and stratosphere) and are a product of temperature gradients within the surrounding air. These sources of clear air turbulence can all pose hazards to small Uncrewed Aircraft Systems (sUAS)s and better measurement of these turbulence-generating mechanisms can potentially lead to better prediction and mitigation of the hazards they pose.

35 Many experiments have conducted stratospheric turbulence measurement using balloon-borne instruments (e.g. Wescott et al., 1964; Ehrenberger, 1992; Haack et al., 2014; Alisse et al., 2000; Gavrilov et al., 2005) with previously published studies of stratospheric turbulence dating back to the 1960s (Enlich and Mancuso, 1968). Among the most relevant conclusions from these studies is that stratospheric turbulence tends to form in relatively thin atmospheric layers due to intrinsic static stability at these altitudes. Among the focus of many studies have been to look for for instances of high turbulent kinetic energy dissipation

40 rate, formally defined as

$$\varepsilon = \frac{1}{2}\nu \overline{\left(\frac{\partial u_i'}{\partial x_j} + \frac{\partial u_j'}{\partial x_i}\right)\left(\frac{\partial u_i'}{\partial x_j} + \frac{\partial u_j'}{\partial x_i}\right)} \tag{1}$$

where Einstein notation has been used to indicate the wind velocity components, u_i, and direction components x_i. Here also ν is the kinematic viscosity, $u_i' = u_i - \overline{u_i}$ is the time-dependent fluctuating part of the velocity component, and the overline indicates an average value. The threshold introduced by Enlich and Mancuso (1968) for high ε was $\varepsilon > 10$ mW kg^{-1}. Many

45 studies also compare ε to the local gradient Richardson number

$$Ri = \frac{\frac{g}{\theta_v}\frac{\partial \theta}{\partial z}}{\left(\frac{\partial \overline{u_1}}{\partial x_3}\right)^2 + \left(\frac{\partial \overline{u_2}}{\partial x_3}\right)^2} \tag{2}$$

where g is the gravitational acceleration,

$$\theta_v = T\left(\frac{100000}{P}\right)^{0.2861}(1 + 0.61q) \tag{3}$$

is the virtual potential temperature, u_1 and u_2 are the horizontal components of the wind vector, x_3 is the spatial component opposite in direction to g, q is the water vapor mixing ratio, T is the temperature in Kelvin and P is the pressure in Pascals. The Richardson number is valuable as it is a ratio of the static stability introduced by the density gradient to the magnitude of the mean horizontal velocity shear which can produce turbulence. A critical Richardson number of $Ri = 0.25$, below which turbulence is likely, is commonly used although a range of values $0.25 < Ri < 1$ have also been proposed (Abarbanel et al., 1984; Galperin et al., 2007). Comparison of ε to Ri thus introduces the possibility to: determine if turbulence production is possible; to estimate if the turbulence arose from a convective or mechanical source of turbulence (Söder et al., 2021; Sharman et al., 2014; Kim et al., 2020); and to model the relationship between turbulence in the stratosphere and tropospheric activity (Chunchuzov et al., 2021).

One series of experiments focused on stratospheric turbulence has been the Leibniz-Institute Turbulence Observations in the Stratosphere (LITOS) experiments. The experiments conducted by LITOS (Haack et al., 2014) consisted of balloons equipped with a thermal anemometer specifically intended to measure velocity and temperature fluctuations at high frequency. The resulting measurements were within sub-centimeter resolution, and therefore suitable for resolving the finer scales of turbulence. This experiment reached altitudes up to 30 km, and ε was compared to both Ri and the square Brunt-Väisälä frequency,

$$N^2 = \frac{g}{\theta_v} \frac{\partial \theta_v}{\partial x_3} \tag{4}$$

as a function of altitude. There was a noted increase in ε with altitude and clear correlation between turbulent events and $Ri < 0.25$. However, in some instances turbulent events were also observed where $Ri > 0.25$ although other studies attribute such behavior to the specifics of the Ri calculation, casting question as to its value as an indicator for the likelihood of turbulence development (Galperin et al., 2007; Haack et al., 2014), although later studies suggest that the measurements may have been contaminated by the balloon wake (Söder et al., 2019). LITOS experiments also investigated the phenomenon of tropopause folding, in which a stratospheric intrusion of air sinks below the upper tropospheric jet stream. The observational result was that dissipation rates above the upper-tropospheric jet were three orders of magnitude larger than below it (Söder et al., 2021) with deeper tropopause folds producing more severe turbulence. Additionally, they found that in both cases of medium and deep tropopause folds the the turbulent dissipation rate was three times higher in the upper troposphere front and Richardson number higher in lower stratosphere front. Galperin et al. (2007) explains that the horizontal movement of the vortex structure of the flow can increase the horizontal mixing even when there is limited vertical mixing in the flow.

Remote sensing measurement techniques have also been deployed for turbulence studies, including the of radars to measure the turbulent kinetic energy dissipation rate (Bertin et al., 1997; Fukao et al., 1994; Sato and Woodman, 1982; Barat and Bertin, 1984). A study conducted in 1983 compares the results of in-situ data with radar-determined dissipation rates and found that the radar-determined values are often underestimated due to the low vertical resolution. However, UHF and VHF radars have presented a better prospect to resolve thin layers of clear air turbulence (Barat and Bertin, 1984). In another experiment, using the Arecibo 430 MHz radar with altitude resolution of 150 m was able to detect the thin layers of turbulence in the lower stratosphere (Sato and Woodman, 1982).

Routine crewed aircraft measurements of atmospheric turbulence are also conducted, for example through the use of an in-situ turbulence detection algorithm developed by the National Center for Atmospheric Research (NCAR) and implemented on some 200 aircraft (Sharman et al., 2014) and through Aircraft Meteorological Data Relay (AMDAR) reports generated by in-situ measurement systems on commercial aircraft. These systems generally report the the turbulence intensity using the metric of eddy dissipation rate (EDR), defined as

$$EDR = \varepsilon^{1/3}, \tag{5}$$

which is currently used as a standard for turbulence reporting by the International Civil Aviation Organization (ICAO). In the NCAR EDR calculation, a fully-formed von Kármán inertial subrange is assumed, and the EDR is determined from either vertical-wind measurements, or the aircraft's gust response measured through acceleration.

Recently, it has become increasingly common to use sUAS equipped with in-situ sensors (e.g. hot-wire anemometers, sonic anemometers, hot-film probes, pitot tubes, or multi-hole pressure probes) for studies of turbulence in the atmospheric boundary layer and troposphere (e.g. Egger et al., 2002; Hobbs et al., 2002; Balsley et al., 2013; Witte et al., 2017; Rautenberg et al., 2018; Bärfuss et al., 2018; Jacob et al., 2018; Bailey et al., 2019; Al-Ghussain and Bailey, 2022; Lawrence and Balsley, 2013; Balsley et al., 2018; Reuder et al., 2012; Calmer et al., 2018; Luce et al., 2020; Kantha et al., 2017). Many of the sUAS used for turbulence studies employ multi-hole probes, which measure the dynamic pressure of the air, with multiple pressure ports combined with a directional calibration to determine the wind vector relative to the probe axis. Due to their fragility, hot-wire probes, which measure the convective heat transfer across a very thin heated filament, are usually reserved for short-term scientific studies although they are standard instruments on some sUAS (e.g. Hamilton et al., 2022). The fast response of the hot-wire anemometer allows detailed characterization of the turbulence, for example allowing the measurement of small-scale fluctuations corresponding to turbulent dissipation.

An additional sensing system which has potential to measure clear air turbulence are infrasonic microphones (Cuxart et al., 2015; Shams et al., 2013). These infrasound sensors are capable of detecting acoustic frequencies below 20 Hz and are typically used for seismic detection and marine acoustics. Within the atmospheric boundary layer, the infrasound energy from ground-based arrays has been found to correspond to the turbulent kinetic energy in the atmosphere, particularly when buoyantly-produced convective turbulence is present. The infrasound energy levels also seem to be higher when there were elevated jets or turbulence above the measurement height, which was thought to be caused by the sound generated at higher altitudes reaching the microphones. In balloon-borne measurements, it has been found that it is possible to detect acoustic low frequency signals, such as microbaroms, using sensitive infrasonic sensors (Bowman and Lees, 2015). The advantage of infrasonic sensors for turbulence detection is that acoustic propagation increases at low frequency and low kinematic viscosity (Whitaker and Norris, 2008) which allows propagation over distances ranging between a few hundred to a few thousand of kilometers. For example, an array of ground-based microphones were able to detect clear air turbulence at distances up to 360 km (Shams et al., 2013).

Despite over a century of work in turbulence detection, predicting the production, presence and characteristics of turbulence in the atmosphere is still a significant challenge. Hence, in-situ observations are still invaluable both as a research tool and

for routine observation. However, as balloons advect horizontally with the wind and are unable to maintain a fixed geospatial location, balloon-based approaches would benefit from complementary measurement approaches.

Here, we present results from a study examining the potential of using a balloon-launched stratospheric glider sUAS for turbulence measurement. A glider offers advantages over traditional balloon launches by being able to descend helically from its release point, during which it is able to transect a wide range of scales within any turbulence encountered, and by maintaining a relatively constant location over the surface during its descent. These qualities facilitate the statistical analysis necessary for quantification of non-stationary properties. One drawback of this measurement approach, however, is that the current regulatory environment makes it challenging to deploy this type of sUAS within a national airspace system without securing permission from the corresponding regulatory body, typically requiring additional measures to ensure deconfliction with crewed aircraft. For example, the measurements reported here had to be conducted in restricted airspace which had been closed to crewed aircraft.

In the measurements reported here, the aircraft was equipped both with standard in-situ sensors as well as a novel infrasonic microphone in order to test the potential of using airborne acoustic signatures to remotely detect the presence of turbulence. This configuration was tested in a series of three high-altitude flight tests conducted at Spaceport America in New Mexico U.S.A., conducting measurements from 25 km to 30 km above sea level down to the surface.

The remainder of this manuscript is divided into three main sections: Section 2 describes the aircraft and measurement systems, along with information about the flight location and flight path; Section 3 examines some approaches which can be used to extract turbulence statistics from the data provided by the aircraft, including vertical profiles of different quantities, profiles of the infrasonic microphone response, and horizontal distributions of key quantities; with Section 4 summarizing the main findings from this study.

2 Experiment Description

2.1 Aircraft

Key to this research was the use of the host sUAS platform, the HiDRON H2 (see Fig. 1), operated by Stratodynamics Inc. The HiDRON H2 is a balloon-launched carbon fiber/fiberglass glider sUAS that is capable of autonomous and soaring flight modes. It has a wingspan of 3.8 m and its nominal flight weight is approximately 5.7 kg with the payload. To achieve initial altitudes in excess of 30 km, the HiDRON H2 is launched using latex sounding balloons. Different sizes of balloons were used with 2000 g, 1200 g and 3000 g employed for Flights 1, 2 and 3, respectively. After release, the aircraft is controlled by a UAVOS Inc. autopilot to follow a pre-programmed descent pattern towards a designated landing point. An operator can track the HiDRON H2 position from launch to landing and changes to the flight plan can be made in real time through radio telemetry, which also allows operational parameters to be transmitted to the ground with a range of 100 km. Full telemetry information was produced at 10 Hz by the autopilot for all three flights, including location, ground speed, 6 degree-of-freedom orientation information as well as pressure, temperature and humidity information from the integrated iMet-XF atmospheric sensors. This
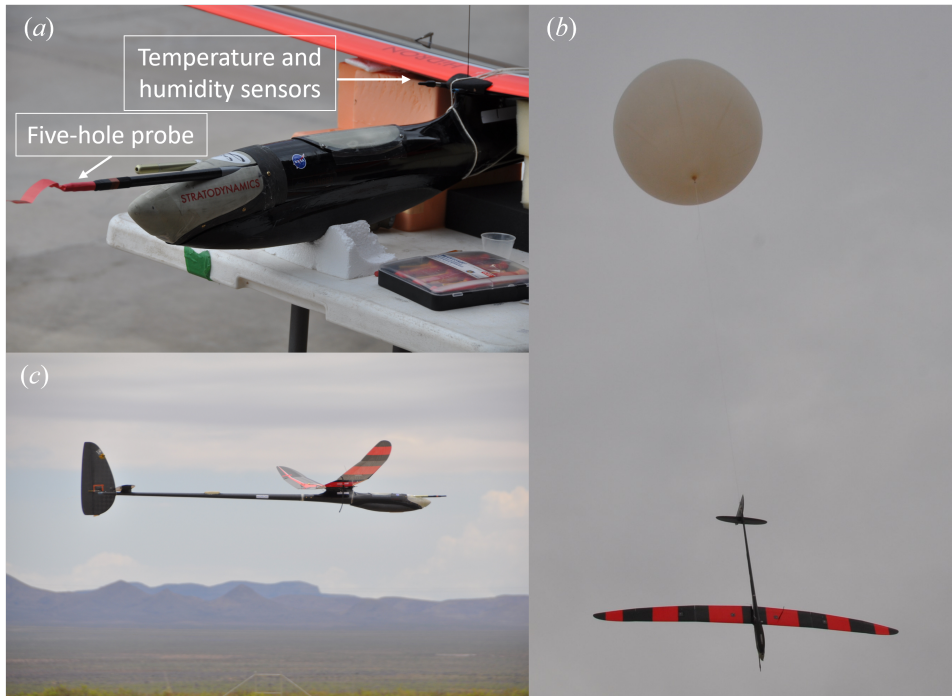
Figure 1. Images of HiDRON H2 showing: (*a*) close up of aircraft nose showing five-hole probe and temperature and humidity sensor location; (*b*) aircraft during launch; and (*c*) aircraft during landing.

10 Hz sample rate telemetry was intrinsic to the radio modem used for the command-and-control link and telemetry. The specific rate was selected for maximum efficiency in the transmission and recording of data packets and to maintain reliability
150 of the radio communication and command-and-control link.

Other safety features include a parachute, dual-redundant balloon release system and geofencing safety protocols that prevent the aircraft from leaving the designated airspace. During prior flights, including flights exceeding altitudes of 30 km, the HiDRON H2 has shown reliability in remaining controllable in high-wind (as high as 32 m s^{-1}), operating in low-temperature conditions ($< -60°$C), and in returning to a predefined landing site.

155 For this flight operation, the autopilot was set to maintain the aircraft's kinetic energy (reflected through the indicated airspeed), with the value selected near the optimal lift over drag ratio (the maximum distance that can be travelled per loss in altitude). To maintain the set airspeed the autopilot adjusts the pitch angle on the elevator to control the angle of attack of the main wing airfoil. The horizontal velocity is a result of setting the airspeed and may fluctuate slightly due to the pitch angle adjustments. Also, as the aircraft descends in altitude the air density increases and the HiDRON's aerodynamic performance
160 improves; thus, the horizontal velocity gradually decreased as the aircraft descended. Figure 2 shows the horizontal speed, $|\boldsymbol{V}_G|$, and descent speed relative to the ground, as well as the magnitude of the aircraft's velocity relative to the wind, $|\boldsymbol{V}_R|$, for each of the three flights. The relative horizontal velocity magnitude was found from $|\boldsymbol{V}_R| = ((V_{G_X} - u)^2 + (V_{G_Y} - v)^2)^{1/2}$ where (V_{G_X}, V_{G_Y}) are the horizontal velocity components of the aircraft relative along the ground to the East and North

respectively and (u,v) are the corresponding horizontal velocity components of the wind, with the method used to obtain the wind velocity vector provided in Section 2.2.
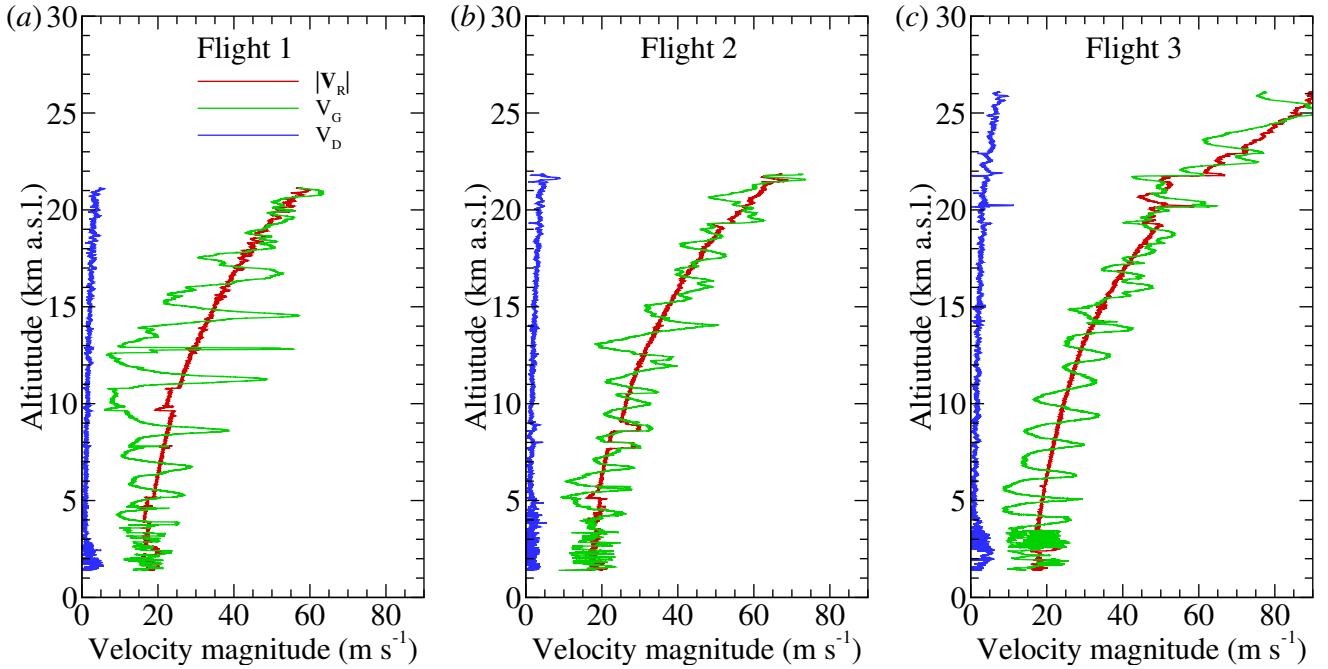
Figure 2. Horizontal ground speed in inertial Earth-fixed coordinates, $|V_G|$, magnitude of the descent speed in inertial Earth-fixed coordinates and relative air velocity magnitude in aircraft-fixed coordinates, $|V_R|$, for (a) Flight 1, (b) Flight 2 and (c) Flight 3.

To measure atmospheric conditions, the aircraft was equipped with an integrated InterMet Systems iMet-XF system having fast-response bead thermistor air temperature, T, and capacitive relative humidity, RH, sensors. The manufacturer-provided specifications (International Met Systems) state the pressure sensor provided a ± 1.5 hPa accuracy for pressure, P, with humidity sensor supporting a full 0 - 100 %RH range at $\pm$ 5 %RH accuracy with a resolution of 0.7 %RH. The temperature sensor provided a $\pm$ 0.3°C accuracy with a resolution of 0.01°C up to a maximum of 50°C. The stated response times of these sensors are on the order of 10 ms for pressure, 5 s for humidity and 2 s for temperature in still air, with the autopilot sampling these sensors at 10 Hz. The pressure and temperature sensors were mounted with the sensing elements exposed to the airflow upstream of the wing support (see Fig. 1a) to ensure sufficient aspiration of the sensors.

2.2   Payload

The turbulence-measuring payload was a combination of four components: (1) a five-hole probe; (2) an infrasonic sensor; (3) a data acquisition board; and (4) an embedded computer. These components were installed in the nose of the HiDRON H2, which could be accessed via removal of the nose cone, as shown in Fig. 3c.
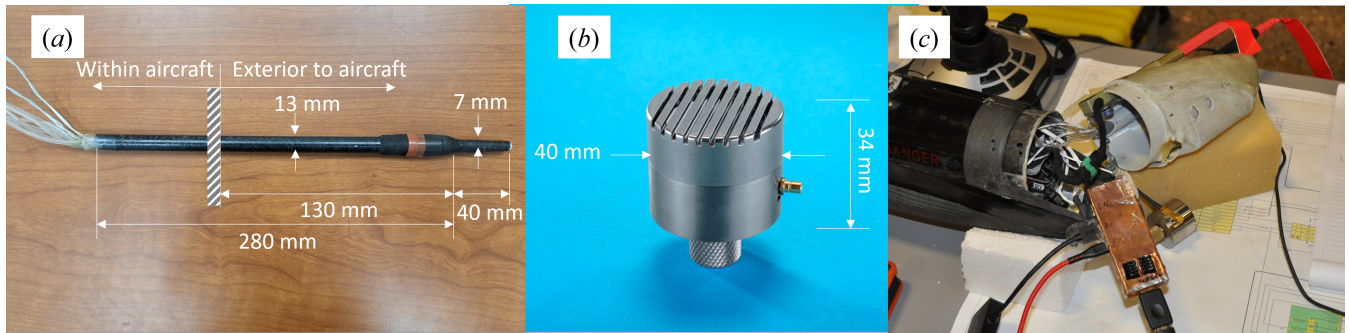
Figure 3. (*a*) Five-hole probe, (*b*) infrasonic microphone, and (*c*) nose payload bay open between flights, with embedded computer shown removed for data retrieval. Infrasonic microphone is below embedded computer but was installed in aircraft nose facing forward during flight.

2.2.1 Five-Hole Probe:

Wind speed and direction relative to the aircraft were measured using a bespoke five-hole probe mounted such that the probe projected upstream of the nose of the aircraft, as shown in Fig. 1. The probe, detailed in Fig. 3a, is similar to that used in Bailey et al. (2019, 2020); Al-Ghussain and Bailey (2022) and was manufactured from a carbon-fiber tube equipped with a beveled aluminum tip. The tip of the probe was arranged with one center hole normal to the probe axis surrounded by four other holes arranged symmetrically around the center hole with their plane normal vector aligned $20°$ to the probe axis. For this measurement, the pressure difference between the central hole (measuring total stagnation pressure) and a series of additional holes arranged on the carbon fiber tube (measuring static pressure) were used to determine the approximate dynamic pressure at the probe tip. The two horizontally-opposed circumferential holes are arranged to produce a pressure difference which changes with the horizontal angle of the wind vector relative to the probe axis. Similarly, the two vertically-opposed circumferential holes were arranged to produce a pressure difference which changes with the vertical angle of the wind vector relative to the probe axis. Prior to installation on the HiDRON H2, the probe was calibrated to determine its directional response in a wind tunnel using an apparatus designed to pitch and yaw the probe at angles up to $25°$ relative to the mean wind vector.

The probe used on these flights was also heated to prevent ice formation within the probe during flight. This was accomplished by wrapping the probe body in nickel-chromium resistance wire. A feedback circuit, using a thermistor attached to the probe tip, passed current through the wire at a rate sufficient to maintain the probe tip temperature at $50°C$. Comparison of wind tunnel directional response calibrations with and without heating active indicated that there was no influence of probe heating on the pressure differences produced, or their dependence on the pitch and yaw angles the probe was exposed to during calibration.

Each hole on the probe was connected to differential pressure transducers through 50 cm of 1.75 mm diameter flexible polymer tubing. Two transducers were used to measure the horizontal and vertical pressure differences across the horizontally and vertically aligned holes, respectively. The third transducer was connected to the central hole, and measured the difference between that hole and static ports on the tube body. To ensure that the low-density conditions at flight altitude did not result in pressure differences below the sensitivity of an individual transducer, the measured pressure difference was converted to

analog voltage using two different sets transducers by teeing the tubing to each transducer sets. The low-sensitivity transducer set was comprised of TE Connected Measurements 4515-DS5A002DP differential pressure transducers with a 500 Pa range. The second transducer set was comprised of Allsensors DS-0368 differential pressure transducers with a 65 Pa range. Both

205 sets of analog output voltages were linearly scaled relative to the maximum transducer range with a nominal span of 4.5V and 4.0V respectively. During flight, the autopilot maintained flight speeds sufficient to produce pressure differences well within the range of the low-sensitivity transducers (i.e. the dynamic pressure was maintained between 100 Pa and 200 Pa) and hence only the readings from these sensors were used for this analysis.

Based off of established procedures, e.g. as outlined by Treaster and Yocum (1978); Bohn and Simon (1975); van den

210 Kroonenberg et al. (2008) and Wildmann et al. (2014), and utilizing a calibration and implementation approach very similar to that used by Witte et al. (2017), the pressure differences at each yaw and pitch angle combination experienced during directional response calibration were used to build pressure coefficients

$$C_\beta = \frac{\Delta P_{32}}{\Delta P_1 + 0.5(\Delta P_{32} + \Delta P_{54})} \tag{6a}$$

$$C_\alpha = \frac{\Delta P_{54}}{\Delta P_1 + 0.5(\Delta P_{32} + \Delta P_{54})} \tag{6b}$$

$$C_q = \frac{\Delta P_1 - Q}{\Delta P_1 + 0.5(\Delta P_{32} + \Delta P_{54})} \tag{6c}$$

where ΔP_1 is the pressure difference between the central hole and the static pressure, ΔP_{32} is the pressure difference across the horizontal probe holes, ΔP_{54} is the pressure difference across the vertical probe holes and Q is the dynamic pressure.

220 The probe design resulted in unique combinations of C_α and C_β for each yaw and pitch angle of the probe relative to the wind vector, with the relationship between C_α and C_β thus derived from the wind-tunnel calibration. The same calibration procedure was used to determine the relationship between C_q and Q. To determine the velocity vector relative to the probe axis experienced during flight, C_α and C_β were calculated for every measurement point and the unique combination used to determine the wind vector angle relative to the probe axis. The corresponding value of C_q measured at that relative angle

225 allowed Q to be determined from the measured ΔP_1. The result is knowledge of the magnitude and direction of the dynamic pressure vector relative to the probe axis. This was then converted to velocity using the density determined from iMet-XF measurements of the ambient pressure, temperature and humidity.

To convert the velocity vector magnitude and direction relative to the probe axis into a frame of reference relative to the ground, an additional coordinate transformation was conducted using the aircraft's pitch, yaw, and roll angles as measured

230 by the autopilot. Details of this process are provided in Witte et al. (2017) and are based off of procedures described in Lenschow (1972) for measurements using similar probes mounted on crewed aircraft. An additional estimate and correction

of the misalignment of the probe axis and aircraft's body-frame axis, airframe influence on the probe, and time misalignment between sensors, was conducted following the approach described in Al-Ghussain and Bailey (2021). The resulting time-dependent wind velocity vector is described using components $u(t)$, $v(t)$, and $w(t)$ which are aligned to the east, to the north, and up, respectively. The time-dependent horizontal wind velocity magnitude and direction were then found from

$$U(t) = \left(u(t)^2 + v(t)^2\right)^{-0.5} \tag{7}$$

and

$$\gamma(t) = \text{atan2}\left(-u(t), -v(t)\right) \tag{8}$$

where atan2 indicates a numerical implementation of the $\tan^{-1}$ function used to disambiguate the polar direction using the quadrant formed by the sign of the velocity components.

As the autopilot and payload data acquisition systems were acquired asynchronously, alignment of autopilot kinematic data and five-hole-probe pressure data in time was conducted during post-processing by cross-correlating the dynamic pressure measured by the aircraft's intrinsic pitot probe (recorded by the autopilot along with the aircraft position and orientation information) and the dynamic pressure measured by the difference between the central port of the five-hole probe and the static pressure ports (recorded by the payload data acquisition system). The time lag between the two systems was then removed before performing the transformation of the velocity vector in the aircraft body frame to the Earth-fixed frame of reference. To do so, the aircraft position and orientation information was up-sampled from the autopilot's 10 Hz sample rate to the 1 kHz sample rate used by the on-board data acquisition system, with the up-sampling conducted using simple linear interpolation. Note also that, although data was acquired at a 1 kHz sample rate, the actual probe frequency response was estimated to be on the order of 20 Hz using the same measurement approach utilized in Witte et al. (2017), which measures the response of the system following a step change in pressure. The limitation in frequency response is caused by viscous attenuation of the pressure fluctuations within the tubing, coupled with inaccuracies introduced by high-frequency resonance within the transducer cavity.

Finally, it should be mentioned that a pressure line was inadvertently disconnected during maintenance prior to Flights 2 and 3, requiring the conversion of five-hole probe voltages to wind for these flights to take a slightly different approach. For these flights, the calibration was updated such that C_α was set to zero and the data processed without the missing transducer. As C_α has primary importance in determine the pitch angle of the flow relative to the probe axis, this value was replaced using the angle of attack determined by the aircraft's autopilot, specifically the angle between the true airspeed determined from the aircraft's pitot probe, and the vertical velocity determined by the aircraft's variometer. To verify that this approach was justified, the Flight 1 data was processed with the original and revised approach, and the impact on the results on the resulting wind velocity statistics found to be negligible, although some differences in the frequency content of the vertical wind component could be expected.

2.2.2 Infrasonic Microphone:

A property of infrasound particularly favorable to the objectives of the proposed work is that it propagates over long distances with little attenuation. Hence, infrasonic measurements of acoustic frequencies below 20 Hz were conducted using an infrasonic microphone. For these tests an extremely low frequency microphone and acoustic measurement system developed at NASA Langley Research Center (LaRC) was used. The microphone, shown in Fig. 1b, was capable of infrasound detection in a portable and easily deployable form factor. Low bandwidth and high sensitivity of the microphone was realized through a high diaphragm compliance (low diaphragm tension) and a large diaphragm radius. The geometry of the microphone was designed such that membrane motion was substantially critically damped and optimally dimensioned for the 0.01 Hz to 20 Hz frequency range. A signal-conditioning unit amplified the microphone output to a ± 10 V full-scale output.

The microphone was mounted rigidly within the nose of the aircraft with the diaphragm facing forward. Being within the fuselage, the microphone was protected by dynamic pressure fluctuations. As the wavelengths of infrasonic sound waves exceed 10 m, sound attenuation by the fuselage was not expected.

2.2.3 Data Acquisition:

A Measurement Computing Systems MCC USB-1608FS-Plus data acquisition system (DAQ) was used to digitize the voltage output from the six pressure transducers and microphone signal conditioning unit. This particular unit was capable of recording eight single-ended analog inputs simultaneously at 16-bit resolution at rates of up to 400 kHz. During these experiments the DAQ sampled seven channels containing the pressure transducer and infrasonic microphone analog voltage signals at 1 kHz for each channel, sending the resulting digitized values to the embedded computer for logging. The DAQ also provided the 5 V signal used to power the pressure transducers.

2.2.4 Embedded Computer:

The DAQ was connected via universal serial bus (USB) to a mini stick computer with an Intel Atom Z8350 processor, 128GB eMMC non-volatile memory, and 4GB RAM. To minimize radio frequency interference and shield the computer from high altitude radiation, the computer was encased in a copper shield (Fig. 3c). A custom script was used to control data acquisition and storage. The computer stored all recorded data on its eMMC memory which was then downloaded post-flight via USB connection for archiving and further analysis. To allow payload operational verification, an RS232 connection was established between the computer and the autopilot. Through this channel, sensor voltage variance and preliminary turbulence detection parameters were passed to the autopilot to be included in the telemetry stream. This information was later available for preliminary temporal alignment of sensor and autopilot data.

2.3 Uncertainty Estimation of Wind Measurement

As described above, the wind measurement was a multi-step process, involving information from multiple sensors combined through application of results from a directional calibration and corrections applied in post-processing. Therefore, to assess the

Table 1. Bias and precision errors for each sensor value used in wind estimate

Measured value	E_B	E_P
$\Delta P_1, \Delta P_2, \Delta P_3$	5 Pa	2 Pa
P	150 Pa	1 Pa
T	0.3 °C	0.01 °C
RH	5%	0.7%
yaw	0.2°	0.01°
pitch	0.2°	0.01°
roll	0.2°	0.01°
V_{G_X}, V_{G_Y}	0.1 m s^{-1}	0.02 m s^{-1}

uncertainty of the wind vector measurement, a Monte-Carlo method was used to estimate the error propagation from the sensors
to the final wind estimate. To do so, the post-processing calculations were repeated for 100 iterations where for each iteration
the sensor values were perturbed from their measured value by an amount determined using normally distributed random
number generators, with the standard deviations of the distributions corresponding to the corresponding sensor uncertainties.
Specifically, for a measured sensor value, here represented as $\Phi(t)$, a perturbed value $\Phi_i(t)$, was found for each iteration, i,
following

$$\Phi_i(t) = \Phi(t) + E_B \mathcal{N} + E_P \mathcal{N}(t) \tag{9}$$

where $\mathcal{N}$ represents a normally distributed random number generator, providing a random scalar drawn from the standard
normal distribution having mean of zero and standard deviation of unity. The quantities E_B or E_P represent the estimated
bias (accuracy) and precision (resolution) errors for the sensor being perturbed, with the bias error perturbation, $\mathcal{N}$, added to
$\Phi(t)$ only once per iteration, and the precision perturbation, $\mathcal{N}(t)$, added for every sample in time. As E_B and E_P are taken
to represent the 95% uncertainty range, but are being used to estimate the standard deviation of the normal distribution, Φ_i
will actually be overestimate the perturbations due to uncertainty. This is done to provide a margin to account for error sources
either under-estimated or not included in the analysis.

The analysis produced an ensemble of 100 time-dependent (and hence altitude-dependent) measurements of wind for each
flight, randomly distributed via the propagation of the perturbed sensor readings, each perturbed following equation 9. The
uncertainty estimate was then found for the resulting wind value using twice the ensemble standard deviation at each measure-
ment time, t, (corresponding to a 95% probability) of the 100 iterations. Note that this approach is similar to that employed by
Van den Kroonenberg et al. (2008), but by employing the Monte-Carlo analysis this approach allows the uncertainty to vary in
time and allows for additional uncertainty due to coupling of sensor errors.

The values for E_B and E_P used in the uncertainty propagation analysis are provided in table 1 and required a a variety
of approaches to determine. For the pressure differences measured by the transducers connected to the five-hole-probe (ΔP_1,

ΔP_2, ΔP_3), E_B was estimated from the average difference between the low-sensitivity and high sensitivity pressure transducer values (as recorded during the entire flight), whereas E_P was estimated using twice the standard deviation of the difference. For P, T and RH, the manufacturer-provided accuracy and resolution values were used for E_B and E_P, respectively. Finally, the uncertainty of the attitude and heading reference system (AHRS) used by the autopilot was not available, so the values for
320   accuracy and resolution values from a different manufacturer's equivalent AHRS system were used as proxy values.
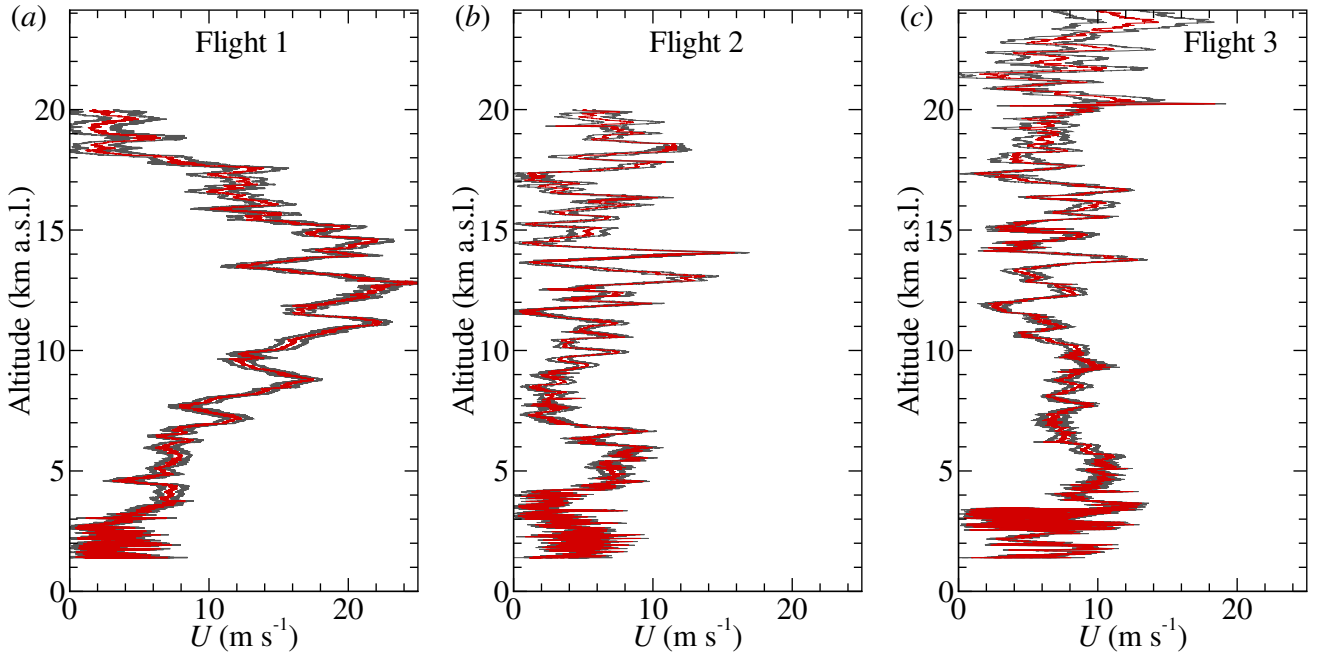
Figure 4. Result of uncertainty analysis for (*a*) Flight 1; (*b*) Flight 2; and (*c*) Flight 3 as red lines. Red lines show velocity magnitude calculated from the mean of 100 ensembles, with corresponding 95% uncertainty bounds shown as black lines.

The mean profiles of wind magnitude produced by the 100 iterations are shown in Fig. 4a-c for Flights 1, 2 and 3, along with the corresponding 95% uncertainty bounds. The uncertainty in the wind estimate was found to be altitude dependent, with the highest uncertainty of approximately 3.5 m s^{-1} observed at the highest altitudes, decreasing to approximately 0.5 m s^{-1} at the lowest altitudes measured. This altitude dependence directly arises from the influence of P, T and RH uncertainty on
325   the air density estimate. Furthermore, although not directly apparent in Fig. 4, the uncertainty in wind magnitude was found to be most dependent on the yaw angle, which is consistent with the observations of Van den Kroonenberg et al. (2008). Note that this analysis does not take into account additional uncertainty introduced by uncertainty in the directional calibration, misalignment in time between the sensors, and any altitude-dependent variability in the values provided in table 1 and therefore the error bounds provided in Fig. 4 should be treated as a rough estimate. As noted previously, to accommodate the undetected
330   uncertainties the E_B and E_P values provided in table 1 are taken to represent the 95% (approximately two standard deviation) error, whereas they are implemented in equation 9 as though they represent the 68 % error bounds (i.e. one standard deviation).

Despite these approximations, we believe that the final uncertainty estimate is reasonable, however, as the probe used in the current study was similar to probes and procedures used in the intercomparison study presented in Barbieri et al. (2019), during which the wind estimates were found to be within $\pm$ 1 m s^{-1} of a ground-based reference velocity sensor.

335 ## 2.4 Experiment Overview
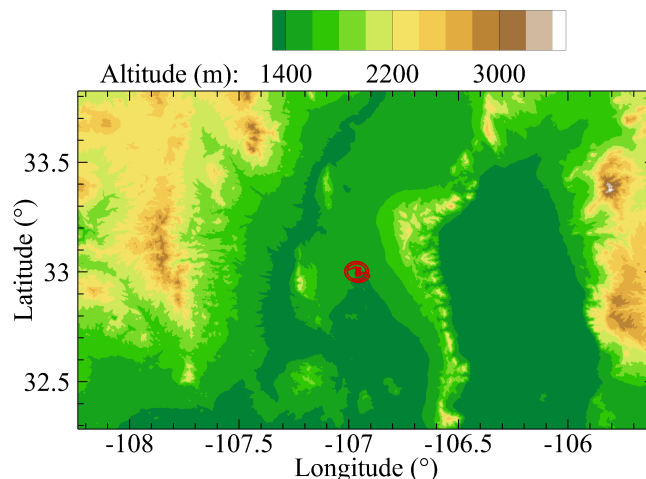
Figure 5. The topography of the flight area with Spaceport America with the trajectory of Flight 3 indicated by a red line to illustrate region of measurement.

The measurement campaign was conducted in the restricted airspace above Spaceport America, located near Truth or Consequences, New Mexico, U.S.A. between the Black Range and San Andres mountain ranges (Fig. 5), from June 1, 2021 through June 6, 2021. Three flights were conducted by the HiDRON H2 on different dates, with Flight 1 being conducted on June 1; Flight 2 conducted on June 4; and Flight 3 being conducted on June 6. Each flight consisted of a weather-balloon carrying the
340 glider aloft to a release altitude of 25 km above sea level (m.s.l.) for Flights 1 and 2, and 30 km m.s.l. for Flight 3 (corresponding to 23.6 km and 28.6 km above ground level, a.g.l., respectively). After release, the aircraft conducted an automated descent along a pre-determined flight path down to the Spaceport America runway.

2.5 Flight Profiles:

The flight trajectories for all three flights are presented in Fig. 6. The flight profiles encompassed balloon launch, ascent to
345 25 km or 30 km altitude m.s.l. at an ascent rate of approximately 7 m s^{-1}, before release of the HiDRON H2 aircraft. The height above sea level of launch and recovery of the aircraft was 1406 m a.s.l.. Once released, the HiDRON H2 conducted a controlled return to the airspace above the launch and control point, whereby it began a spiraling descent at an initial radius of approximately 5 km. This 5 km radius was selected as a comprise between optimizing aerodynamic efficiency of the aircraft in a turn (by minimizing the bank angle) and for safety to stay in proximity to the landing runway. As the aircraft descended,
350 this radius was reduced to approximately 4 km and eventually, 1 km to keep the aircraft close to the designated landing point.

During the descent phase of the flight, as shown in Fig. 2, the rate of descent decreased from 5 m s^{-1} to 1 m s^{-1} (producing a nominal descent rate of 2 m s^{-1}). Overall flight time was approximately 6 hours with 4 hours of that being the descent phase. Autopilot-controlled approach, landing and recovery occurred on the Spaceport America main runway at which point the aircraft, payload and all logged data were recovered.

355   All three flights started in the morning hours, with Flight 1 launched at 13:47 UTC (07:47 LT) on June 1 2021, released from the balloon at 14:35 UTC (08:35 LT), and landing at 18:42 UTC (12:42 LT). Flight 2 launched at 14:04 UTC (08:04 LT) on June 4 2021, released at 15:15 UTC (11:15 LT) and landed at 18:39 UTC (12:39 LT). Finally, Flight 3 launched at 14:07 UTC (08:07 LT) on June 6 2021, released at 15:17 UTC (09:17 LT), and landed at 19:43 UTC (12:43 LT). Local time, LT, at Spaceport America was Mountain Daylight Time (UTC -6:00).
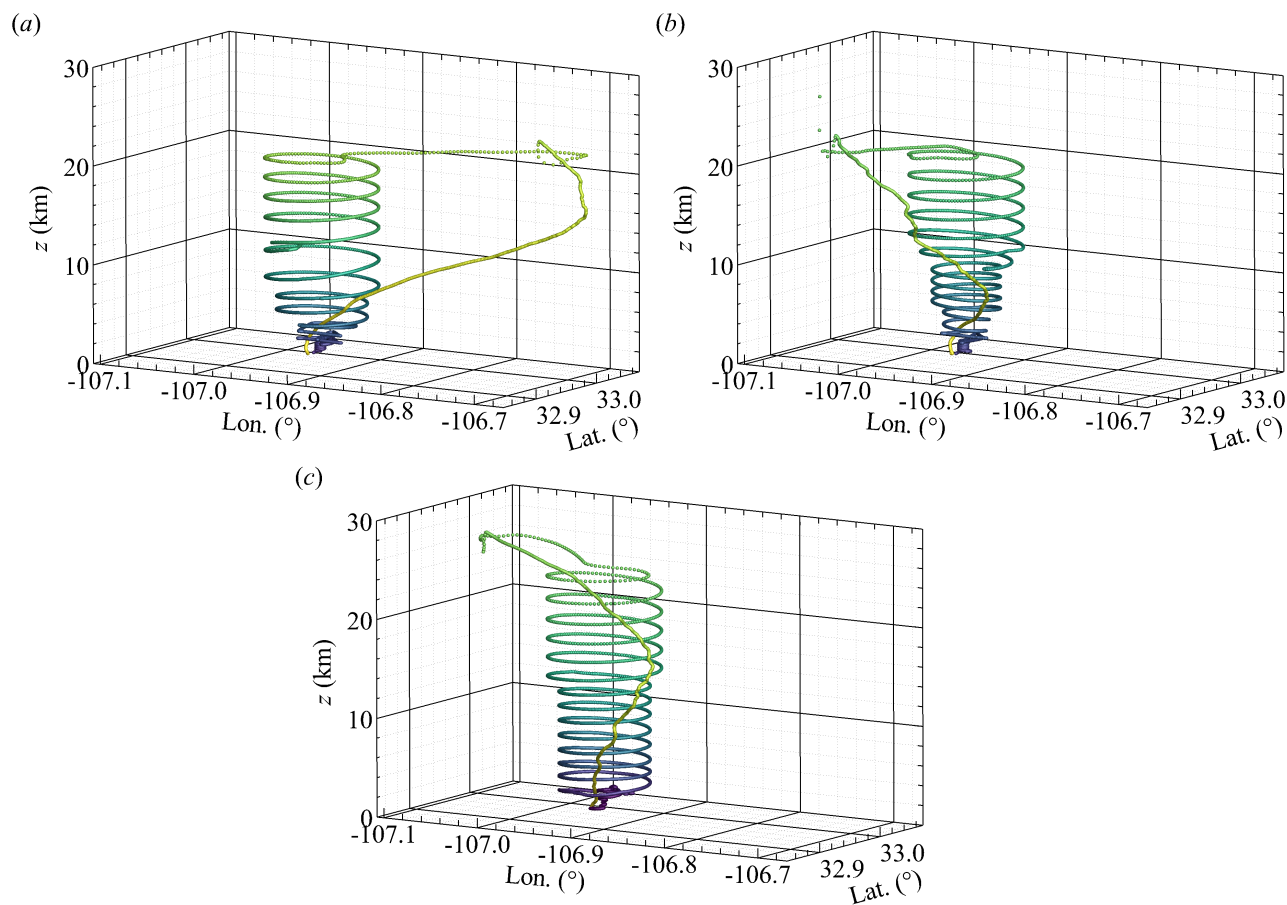
Figure 6. HiDRON H2 flight trajectory for (a) Flight 1, (b) Flight 2 and (c) Flight 3. Trajectory is colored by time, with lighter color indicating earliest phase of balloon ascent. z indicates height above ground level (a.g.l.)

3 Results

In this section, we present the measured values of temperature, relative humidity, wind vector, and infrasonic microphone signal amplitude, and present calculation approaches which can be used to extract different derivative statistics from the measured values. These statistics are presented in the form of vertical profiles in Sections 3.1 to 3.4, and in the form of spatial distributions in Section 3.5. As the temperature and humidity sensors were mounted on the front side of the wing pillar (as shown in Figure 1a), during ascent they were in a stagnant region within the wing pillar wake and therefore not sufficiently aspirated to prevent self-heating and delayed air exchange with the environment. Hence, only data from the controlled descent phase of the flight are presented for temperature and humidity in this section. In addition, z is used to indicate altitudes are referenced to ground level, i.e. above ground level (a.g.l.) with $z = 0$ referencing the launch and recovery altitude of 1406 m a.s.l..

To obtain statistical properties as a function of z, the time-series during descent was divided into 3 km statistical segments, determined using $|\boldsymbol{V}_R|\Delta t$, where Δt is the amount of time included in each segment. Quantities averaged over these segments are indicated using $\langle \ \rangle$ brackets. To increase the spatial resolution of these statistics, each segment is overlapped by 50% (1.5 km). As the separation between each aircraft orbit (Fig. 6) was nominally 2 km, these segment sizes were selected to produce statistical bins of approximately equivalent horizontal and vertical separation. Due to the spiralling flight path (as illustrated in Fig. 6) each 3.0 km segment represents approximately 200 m of vertical descent, with the overlapping of segments reducing the vertical interval to approximately 100 m.

3.1 Mean quantities

To establish the ambient conditions during each flight we averaged P, T, RH, U and γ over each statistical segment and compare vertical profiles of these quantities to publicly-available 12:00 UTC National Weather Service (NWS) radiosonde weather soundings launched from the El Paso (EPZ), Albuquerque (ABQ) and Tuscon (TUS) NWS forecast offices. These forecast offices and sounding times were selected due to their proximity to the launch site and flight times, with the launch site within the triangle formed by these three locations. To assist with comparison across sites in z, we have set $z = 0$ to 1406 m a.s.l. for all profiles. Furthermore, to assist with comparison, the National Oceanic and Atmospheric Administration (NOAA) upper air maps at 250 mb and National Aeronautics and Space Administration (NASA) satellite imagery for the approximate time of Flights 1 through 3 are provided in Appendix A with the NWS sounding sites and HiDRON H2 flight location indicated on them. The NWS soundings employed Graw DFM-17 radiosondes with manufacturer provided accuracies of $\pm0.2°C$ in temperature, $\pm4\%$ in RH, ±0.1 m s^{-1} in wind speed and $\pm1°$ in direction.

Vertical profiles of $\langle T \rangle$ and $\langle RH \rangle$, measured by the HiDRON H2 are compared to the radiosonde profiles for all three flights in Fig. 7. The HiDRON H2 temperature is consistent with the trends produced by the radiosonde values, but shows a noticeable warm bias compared to the radiosonde above $z = 16$ km that appears most noticeable for Flight 3. Note that no density correction was applied to this sensor measurement to account for the reduced convective heat transfer at these altitudes. The lapse-rate in the tropsophere also appears to deviate from the radiosonde lapse rates for $z < 5$ km, although it is not clear if this is due to a sensor-related issue or due to spatial variability in the atmospheric conditions.
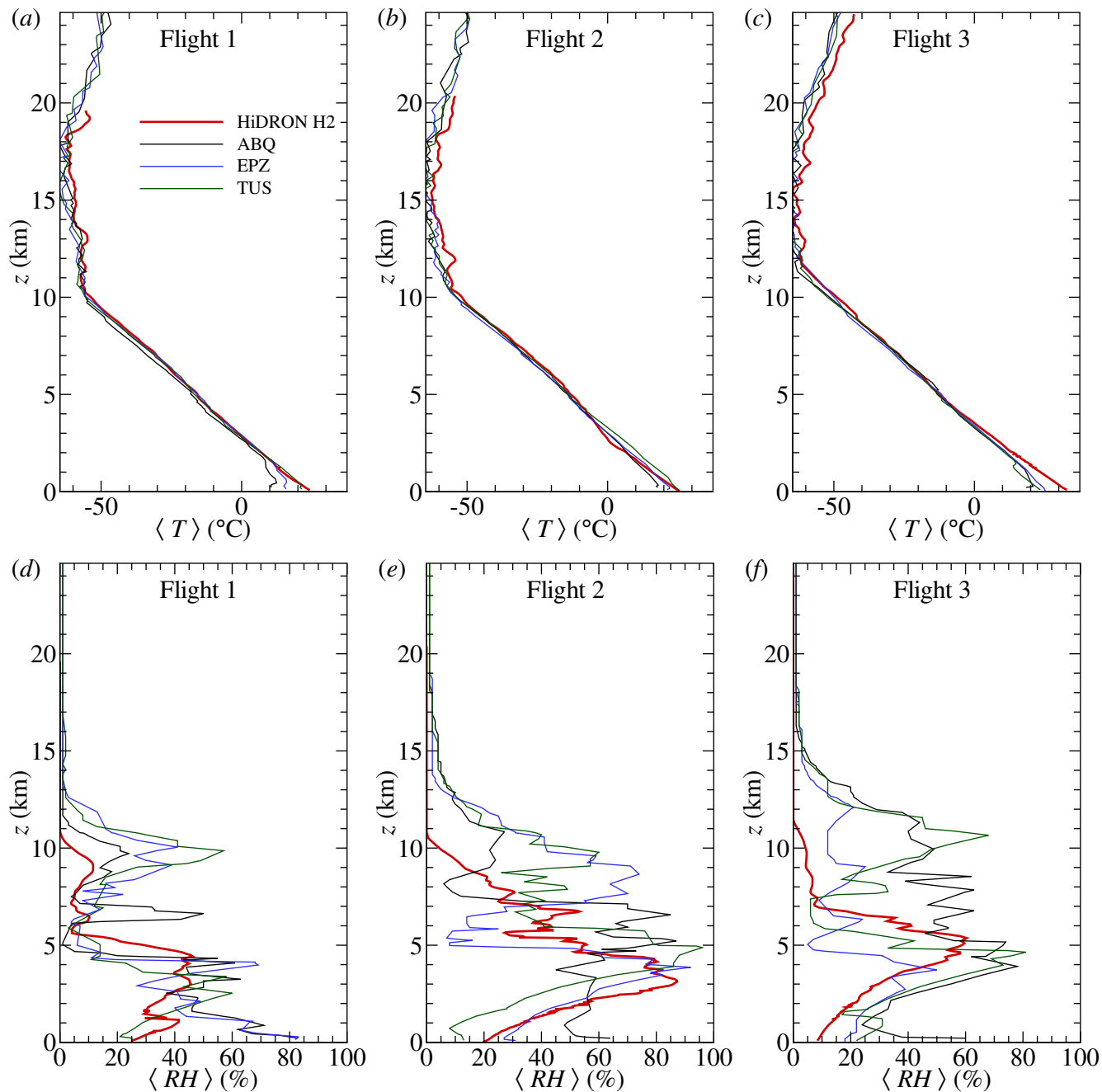
Figure 7. Temperature profiles measured during (*a*) Flight 1; (*b*) Flight 2; and (*c*) Flight 3. Corresponding relative humidity profiles shown for (*d*) Flight 1; (*e*) Flight 2; and (*f*) Flight 3.

Figures 7d-f compare the corresponding $\langle RH \rangle$ measurements from the HiDRON H2 and NWS radiosondes. Significant differences are clearly evident among the profiles. However, noting that the radiosonde data were obtained from disparate
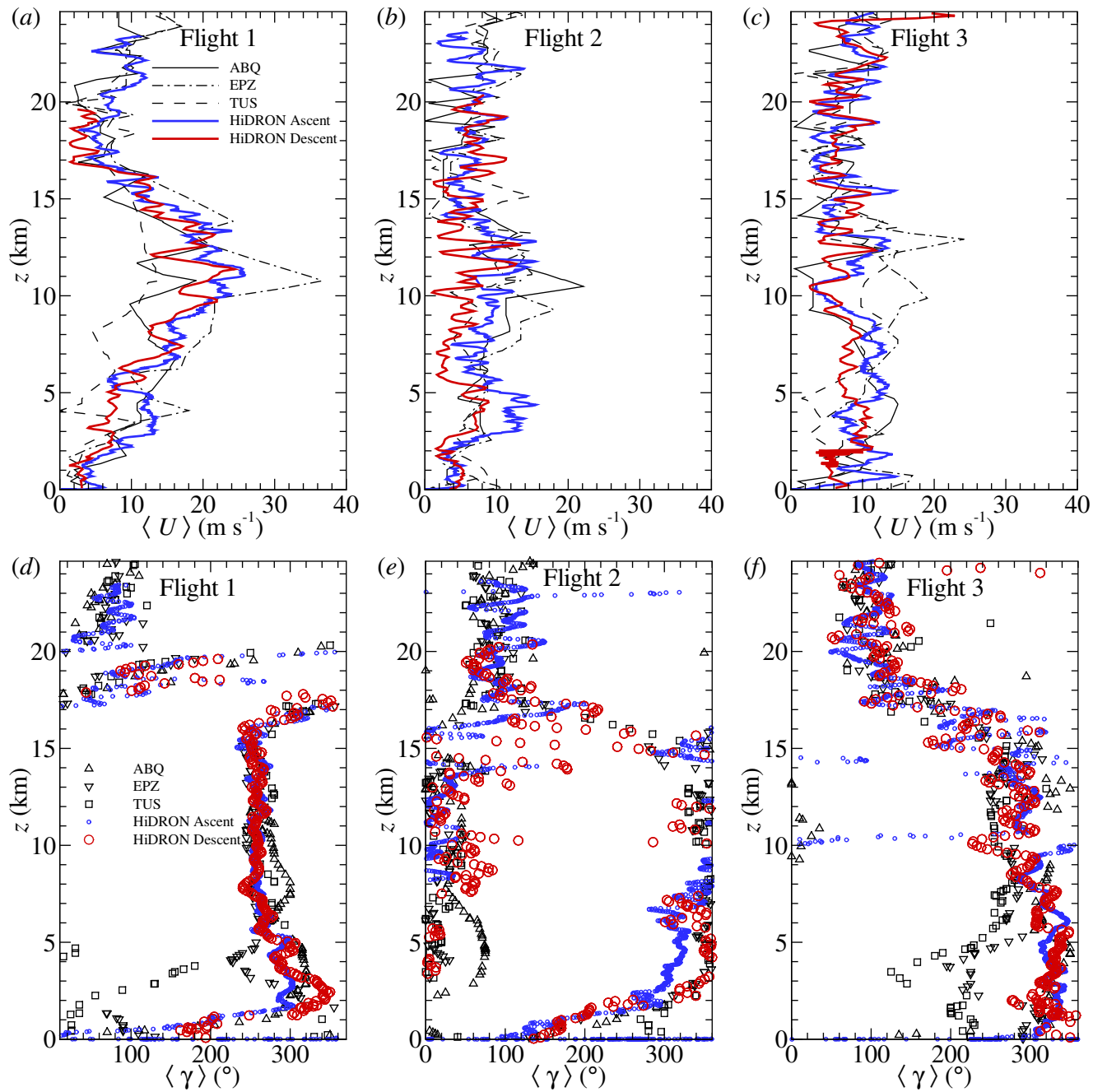
Figure 8. Horizontal wind magnitude a measured during (*a*) Flight 1; (*b*) Flight 2; and (*c*) Flight 3. Corresponding wind direction shown for (*d*) Flight 1; (*e*) Flight 2; and (*f*) Flight 3.

395 locations up to 380 km away from the flight location, differences can be attributed to spatial heterogeneity in the atmospheric

moisture concentration. This is qualitatively illustrated by comparison of the cloud coverage in satellite observations (Appendix A). However, on all three days, the HiDRON H2 reported consistently lower RH values for $z > 7$ km, so a dry bias in the humidity sensor under cold conditions cannot be discounted.

The magnitude and direction of the horizontal winds for all three flights are shown in Fig. 8. In addition to comparison to the radiosonde soundings, we also compare the profiles measured during descent to those estimated from the ascent phase of each flight using the ground using (V_{G_X}, V_{G_Y}), as measured from the onboard GPS. To filter any possible influence of pendulum motion of the aircraft on the balloon tether (estimated to have a natural period of approximately 5 s), the velocity values were filtered by applying a 25 s moving average. The resulting wind estimates are treated as approximately equivalent to those produced by radiosondes, although the significantly increased weight of the aircraft relative to a radiosonde can be expected to produce a corresponding increase in the time constant compared to that of a radiosonde.

In general, the wind magnitude and direction measured by the HiDRON H2 are within the bounds provided by the the radiosonde soundings, with the wind direction measured during descent producing good agreement with that reported by the radiosondes and by the GPS on ascent. With respect to the wind magnitude, the HiDRON measurements do contain higher frequency fluctuations that are evident in the NWS soundings. These high frequency fluctuations were evident in both ascent (GPS ground velocity) and descent (five-hole-probe) velocity measurements made using the HiDRON H2 and are also evident in other high-resolution radiosonde measurements (e.g. Ko et al. (2019)). One significant difference between ascent and descent measurements are stronger low frequency waves measured during descent for Flight 1 in the range $7.5 < z < 12.5$ km and for Flight 2 in the range $11 < z < 13$ km. These low frequency waves may be bias in the wind estimate introduced by the orbital path, but as they far exceed the estimated uncertainty bounds, there source would have to arise from an unaccounted for error. Similar wavelengths are evident in the ABQ wind profile for Flight 1 and therefore an alternative explanation is that they are a consequence of the measurement approach whereby in descent the aircraft is better able to resolve horizontal wind gradients than in ascent, during which the balloon is being passively transported in the horizontal direction by the wind.

Atmospheric conditions were different for Flight 1 when compared to Flights 2 and 3. The strongest winds occurred during Flight 1, with the winds coming from $270°$ and increasing with altitude to a peak value over 20 m s^{-1} just above the tropopause ($z = 12.5$ km), before decreasing with altitude to the stratospheric inversion near $z = 17$ km. This pattern of constant wind direction and high wind magnitude is consistent with the presence of a jet stream, and the NOAA upper air wind meteorological maps Appendix A) indicate that during Flight 1 a tropical jet stream was centered to the southeast of the flight location, over central Texas, such that the flight path was on the outer edge of the jet. The relative position of the jet stream for Flight 1 also explains the higher wind magnitudes measured at El Paso (EPZ), which was closer to the center of the jet. Above the jet stream for Flight 1, the winds increase with altitude again, with significant directionality shift indicating horizontal shear was present above the temperature inversion.

The jet stream had moved to the east by the time of Flights 2 and 3 (as shown in Appendix A), which is reflected in the reduced magnitude of winds measured during these flights and calmer wind conditions were observed (Fig. 8b,e and Fig. 8c,f respectively) with magnitudes typically below $\langle U \rangle = 10$ m s^{-1} measured by the HiDRON H2, consistently from the north for $z < 15$ km for Flight 2, with directional shear observed between $z = 15$ km and $z = 20$ km. Finally, observations during

Flight 3 indicate nearly constant values of $\langle U \rangle \approx 10$ m s^{-1} up to $z = 30$ km, with winds coming from $300°$ in the troposphere backing with altitude to be from $100°$ at $z = 20 \; km$

3.2 Stability Conditions

Profiles of the square Brunt–Väisälä frequency, N^2, shear frequency, S^2, and gradient Richardson number, Ri, provide some perspective of the atmospheric stratification and static stability, horizontal velocity shear, and potential for turbulence generation. The square Brunt–Väisälä frequency reflects the static stability and was estimated from

$$N^2 = \frac{g}{\langle \theta_v \rangle} \frac{\partial \langle \theta_v \rangle}{\partial \langle z \rangle}. \tag{10}$$

The square shear frequency can also be found from

$$S^2 = \left(\frac{\partial \langle u \rangle}{\partial \langle z \rangle} \right)^2 + \left(\frac{\partial \langle v \rangle}{\partial \langle z \rangle} \right)^2 \tag{11}$$

and provides a measure of the possibility of turbulence production by vertical wind shear. The corresponding gradient Richardson number can therefore be found from

$$Ri = \frac{N^2}{S^2}. \tag{12}$$

The helical descent of the aircraft results in approximately 1500 m of horizontal travel for every 100 m of decent and creates some ambiguity in determining the vertical gradients of $\langle \theta_v \rangle$, $\langle u \rangle$ and $\langle v \rangle$. If we assume horizontal homogeneity of $\langle \theta_v \rangle$, $\langle u \rangle$ and $\langle v \rangle$ then the vertical gradients can be calculated between neighboring 1500 m statistical segments in time, resulting in a 100 m resolution in the gradient. The profiles of $N = \sqrt{N^2}$ and $S = \sqrt{S^2}$ calculated in this manner (using central differencing between time-adjacent statistical segments) are referred to as N_t and S_t and shown in Fig. 9a-c and Fig. 9d-f for all three flights respectively. The results show large oscillations with altitude for all three flights. These oscillations are introduced by horizontal variability in $\langle u \rangle$, $\langle v \rangle$ and $\langle \theta_v \rangle$ between each segment (nominally 1500 m) which are amplified by the relatively small difference in $\langle z \rangle$ between each segment (typically around 100 m).

An alternative approach was therefore devised to calculate vertical gradient whereby the vertical profiles were expanded along the circumference of the aircraft's orbit, here represented in the form of azimuthal position of the aircraft relative to the center of its orbit, α, which was defined with $\alpha = 0$ directed to the north and increasing positive towards the east. In this manner, $\langle \theta_v \rangle (\alpha, z)$, $\langle u \rangle (\alpha, z)$ and $\langle v \rangle (\alpha, z)$ were determined. The vertical gradient of each quantity was then found by finding the nearest statistical segments in the positive and negative z directions which minimized the difference in α. These three locations were then used to determine $\partial \langle \theta \rangle / \partial \langle z \rangle$, $\partial \langle u \rangle / \partial \langle z \rangle$ and $\partial \langle v \rangle / \partial \langle z \rangle$ for the central statistical segment using central differencing, and the resulting N and S profiles are shown on Fig. 9, with the results calculated using this approach and referred to as N_z and S_z, respectively. Note that this approach is effectively a gradient calculation across a spatial scale of the same order as the vertical separation between orbits, approximately 2.5 km. However, this gradient calculation could
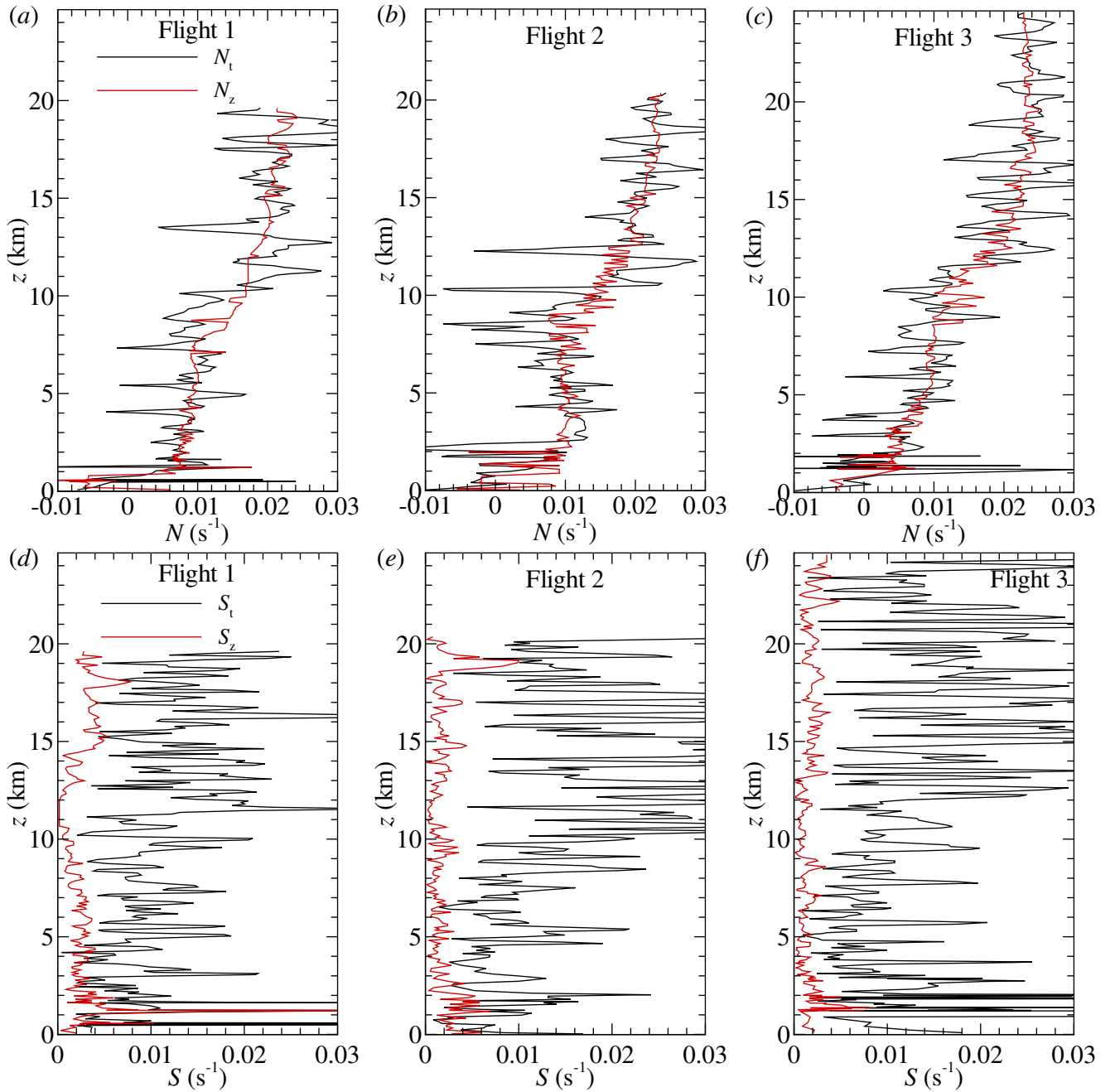
Figure 9. Square Brunt–Väisälä frequency, N_t^2 and N^2, profiles for (*a*) Flight 1; (*b*) Flight 2; and (*c*) Flight 3 and shear frequency, S_t^2 and S^2, profiles for (*d*) Flight 1; (*e*) Flight 2; and (*f*) Flight 3.

460   be conducted for every statistical segment, resulting in a temporal resolution of these values that is the same as N_t and S_t.

Furthermore, unless the statistical segments were reduced in size, this approach could not resolve the gradients in regions where
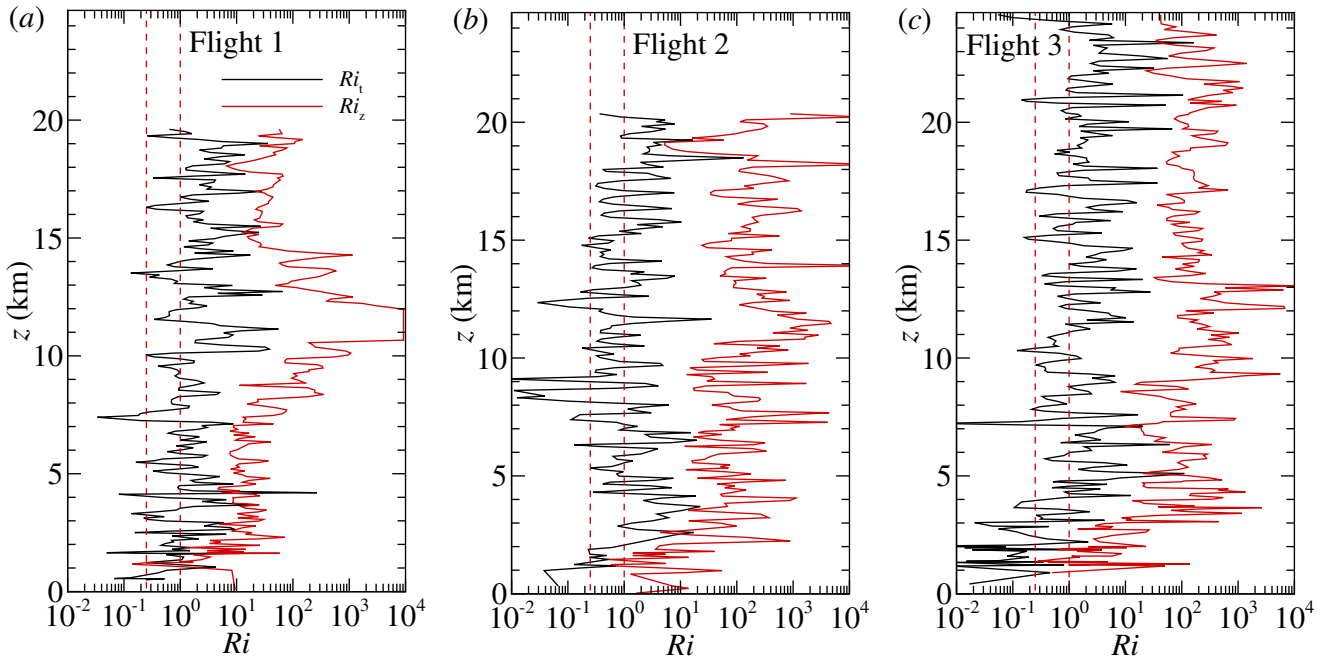
Figure 10. Gradient Richardson number, Ri_t and Ri, profiles for (*a*) Flight 1; (*b*) Flight 2; and (*c*) Flight 3. The vertical lines indicate $Ri = 0.25$ and $Ri = 1$, denoting the possible range of critical Richardson numbers.

the horizontal separation between the segments was on the same order as the vertical separation, specifically for the portion of the flight when the aircraft was in a reduced diameter orbit near the landing point ($z < 1$ km) and for a small segment of Flight 1 near $z = 11$ km when the aircraft briefly executed a smaller orbit during its larger orbit (as shown in Fig. 6a). For this latter region, the values of N_z and S_z are kept constant in Fig. 9.

Fig. 9a-c shows that although the N_t and N_z profiles are similar, there are fewer large-scale excursions in N_z. The general trend shows statically near-neutral conditions existed above the boundary layer for Flights 2 and 3, reaching $z = 3$ km for Flight 3. For the remainder of the altitudes measured, the N_z values indicate statically stable conditions existed, with a monotonic increase in N_z with altitude. The corresponding S_z profiles shown in Fig. 9d-f, however, most likely due to the larger vertical distance involved in the differencing, are significantly different in magnitude from their S_t counterparts, being typically an order of magnitude lower. The largest difference was observed during Flight 1 near $z = 11$ km, which corresponds to the height where $\langle U \rangle$ is a maximum, resulting in the central differencing across the jet producing mean velocity gradients near zero.

The resulting profiles of Ri are shown in Fig. 10a-c for Flights 1 through 3, for both $Ri_t = N_t^2/S_t^2$ and $Ri_z = N_z^2/S_z^2$. For comparison a possible critical Richardson number range of $0.25 < Ri < 1$ (Abarbanel et al., 1984; Galperin et al., 2007) is also illustrated on the figures which affirms that the measured Ri is consistently above this range. These results indicate that whereas, in general $Ri_t < 10$ with frequent instances of $Ri_t < 1$, $Ri_z > 10$ for the majority of the profile, with low and

negative Ri_z measured only in the region near the boundary layer. Again, this roughly two-orders-of-magnitude difference in Ri_t and Ri_z values can be attributed to the order of magnitude difference in S_t and S_z.

480   **3.3   Turbulent Quantities**

The results presented in the previous section indicated that statically stable conditions predominated during all three flights, with the N_z and Ri_z profiles suggesting conditions were conducive to buoyant turbulent production only near the boundary layer. However, S_t, Ri_t and S_z values were occasionally measured in the stratosphere that suggest the potential for turbulent production due to shear instabilities and gravity wave breaking in the stratosphere.

485   The nature of the HiDRON H2 measurements allows the determination of different metrics that can be used to confirm the presence of turbulence at different altitudes. One measure of the local turbulence intensity is the turbulent kinetic energy, k. Here, k was calculated as a function of distance along the flight trajectory using

$$k = \frac{1}{2}\left(\langle u'^2 \rangle + \langle v'^2 \rangle + \langle w'^2 \rangle\right) \tag{13}$$

where, $u'(t) = u(t) - \langle u \rangle$, with equivalent definitions for $v'(t)$ and $w'(t)$. Note that since $u(t)$, $v(t)$ and $w(t)$ were oversampled,
490   to minimize the influence of high frequency noise on these quantities, $\langle u'^2 \rangle$, $\langle v'^2 \rangle$ and $\langle w'^2 \rangle$ were calculated by first subtracting $\langle u \rangle$, $\langle v \rangle$ and $\langle w \rangle$ from u, v and w, respectively, then calculating the velocity spectrum of each velocity component in the frequency domain for each statistical segment of the time series (here denoted as $F_{uu}(f)$, $F_{vv}(f)$ and $F_{ww}(f)$ respectively, where f is frequency). This was done using Welch's periodogram method implemented with a variance-preserving Hanning window, three subintervals, and a 50% overlap. The low-pass filtered estimates of $\langle u'^2 \rangle$, $\langle v'^2 \rangle$ and $\langle w'^2 \rangle$ were then determined
495   by integrating $F_{uu}(f)$, $F_{vv}(f)$ and $F_{ww}(f)$ over the range $f < 20$ Hz. This threshold was selected to coincide with the maximum frequency at which the probe's response to pressure fluctuations response could be expected to be unity. The resulting profiles of k for all three flights are presented in Fig. 11a-c.

     For Flight 1 the boundary layer turbulence is clearly evident in Fig. 11a as an increase in k for $z < 2$ km, with slightly thicker regions of elevated k evident in Fig. 11b and c for $z < 4$ km and $z < 3$ km for Flights 2 and 3. Above these altitudes, the values
500   of k largely remained below unity except in several localized regions where elevated k values were measured. For Flight 1 within the troposphere, these regions occurred at $z \approx 3$ km, 6 km and $z \approx 8$ km, whereas within the stratosphere broadly elevated values of k were observed for $z > 16$ km, with significant increase in k observed at $z = 11.5$ km. Similar behavior was measured during Flights 2 and 3, specifically $k > 1$ near the surface, and isolated and localized regions of enhanced k within the troposphere and stratosphere, although these cases exhibit generally higher k and more variability in the profiles.

505   Note that the elevated values of k may not necessarily correspond to velocity fluctuations caused by turbulence. To assess the presence of an inertial subrange corresponding to the existence of a universal equilibrium range within the turbulence, we examine the one-dimensional energy spectra in wavenumber space, here estimated from the longitudinal velocity spectra using the relative velocity of the air relative to the sensor. This velocity spectrum was calculated by first rotating the (u, v, w) coordinate system from the east-north-up alignment to instead align u with an axis parallel to the velocity of the aircraft within
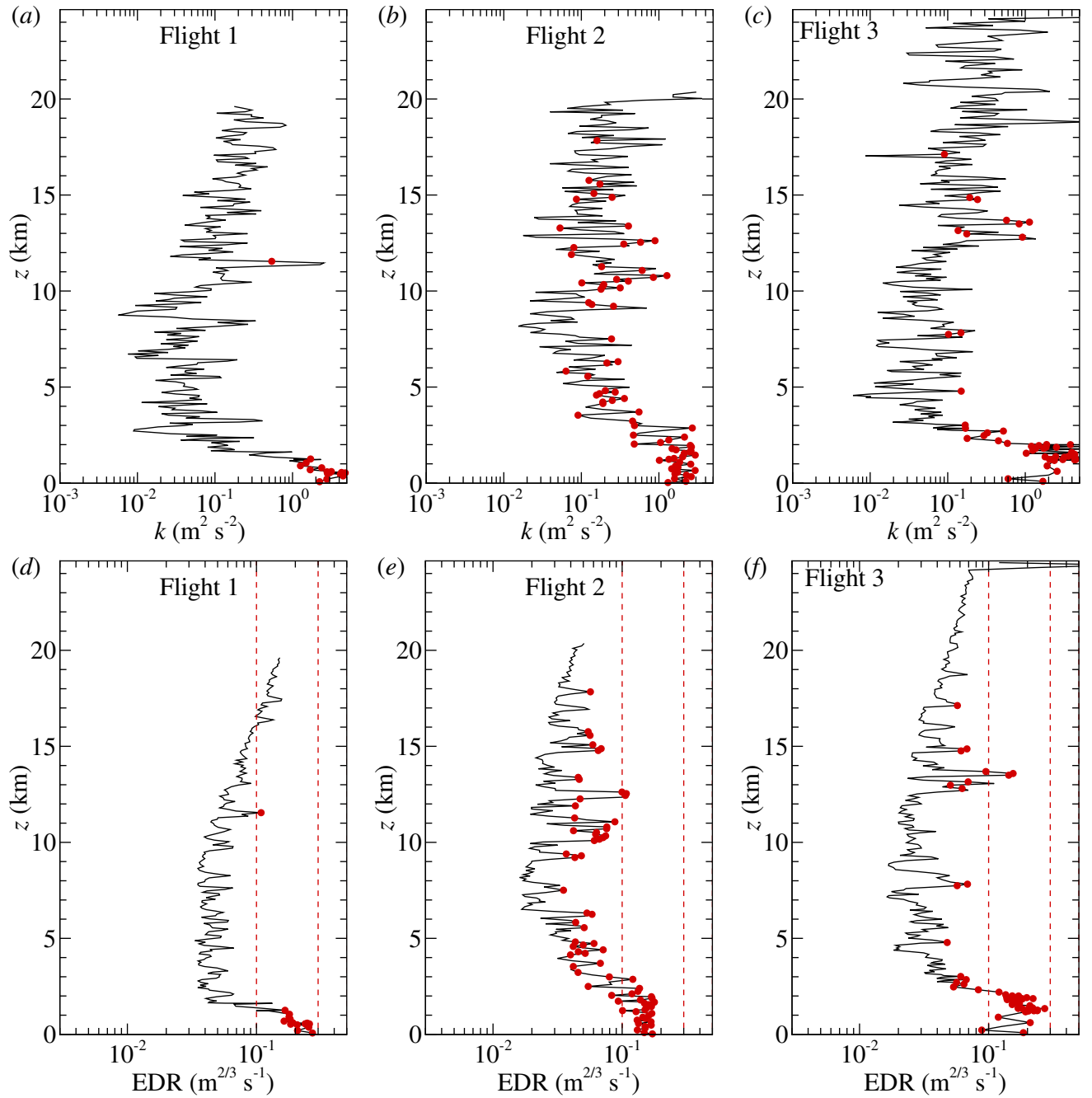
Figure 11. Profiles of k for (a) Flight 1, (b) Flight 2, and (c) Flight 3. Corresponding profiles of EDR are shown for (d) Flight 1, (e) Flight 2, and (f) Flight 3. Solid red symbols indicate measurements where $-1.8 < n < -1.5$. Dashed lines indicate qualitative turbulence intensity levels from Huang et al. (2019) referred to as: steady for $EDR < 0.1$; weak for EDR between 0.1 and 0.3; moderate for EDR between 0.3 and 0.5; strong for EDR between 0.5 and 0.8; and very strong for $EDR > 0.8$.
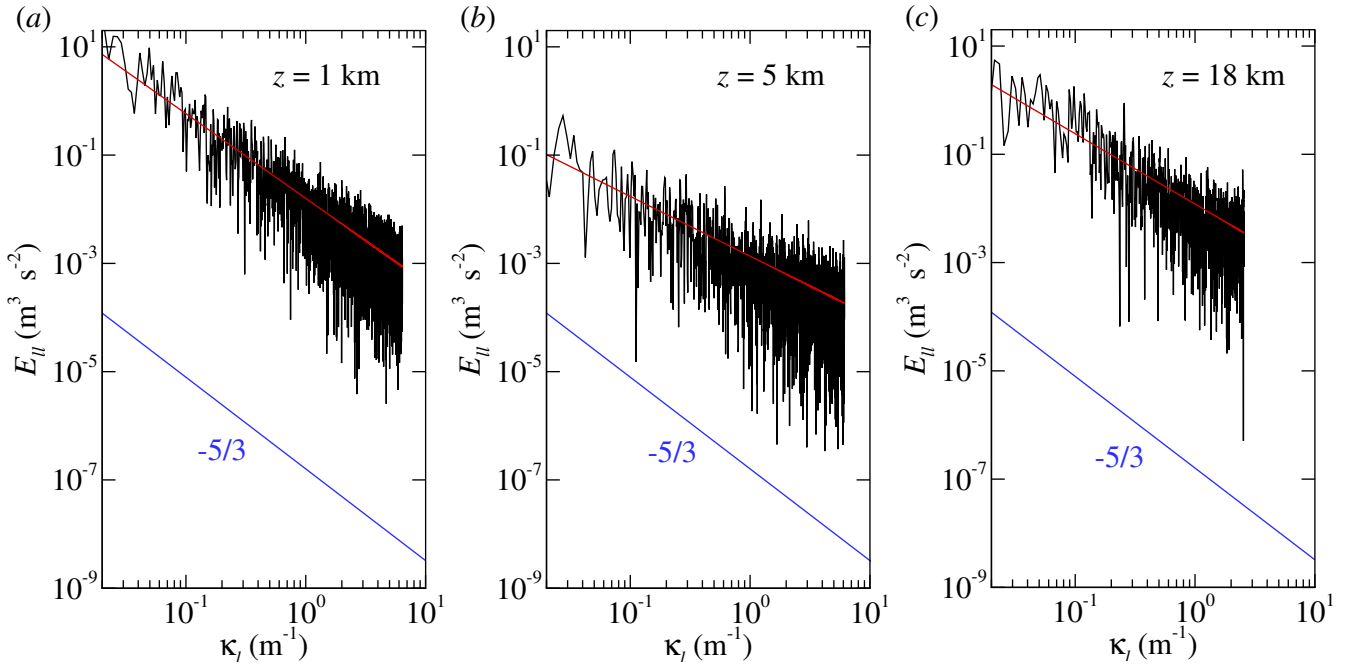
Figure 12. Example longitudinal velocity spectra from Flight 1 at (*a*) $z = 1$ km, (*b*) $z = 10$ km, and (*c*) $z = 18$ km. Red lines indicate fit, blue lines indicate $f^{-5/3}$ slope. Only content for wavenumbers corresponding to $f < 20$ Hz are shown.

510   the air, i.e. we define $u_\ell(t)$ as the component of the wind velocity vector found by projection of the wind velocity vector, $\boldsymbol{U}$,

in the direction formed by $\langle \boldsymbol{V}_G - \boldsymbol{U} \rangle$. The velocity spectrum of $u_\ell(t)$ in the frequency domain, $F_{\ell\ell}(f)$, was calculated on the

rotated wind velocity vector.

     To transform the velocity spectrum in the frequency domain to the wavenumber domain, the longitudinal wavenumber, κ_ℓ,

was then approximated using Taylor's frozen-flow hypothesis such that $\kappa_\ell \approx f 2\pi |\langle \boldsymbol{V}_R \rangle|^{-1}$. We then found the longitudinal

515   velocity spectrum in the wavenumber domain as $E_{\ell\ell} = F_{\ell\ell} |\langle \boldsymbol{V}_R \rangle|(2\pi)^{-1}$, where this last operation was conducted to ensure

that integrating $E_{\ell\ell}(\kappa_\ell)$ in κ_ℓ produced the variance of u_ℓ.

     Example longitudinal velocity spectra in the wavenumber domain are shown in Fig. 12 which demonstrate, as evident in

Fig. 12b,c, that although the spectra indicate a broadband energy content within the five-hole-probe sensor's response range

($f < 20$ Hz), the spectra can display some deviation from the characteristic $-5/3$ slope associated with the locally isotropic

520   turbulence expected within the inertial subrange (Kolmogorov, 1941).

     We then identify instances where a turbulent inertial subrange is present as instances where the power law fit of Bf^n to

$E_{\ell\ell}(\kappa_\ell)$ (in the range $\kappa_\ell > 0.1$ m^{-1}, $f < 20$ Hz) produced exponent values within the range of $-1.8 < n < -1.5$, correspond-

ing to $-5/3 \pm 10\%$. When these instances are isolated (as indicated by solid red symbols in Fig. 11a-c), very few turbulent

regions become evident for Flight 1. However, for Flights 2 and 3 (Fig. 11b and c) this criteria becomes less discriminating,

525   which may correspond to the increased fluctuations in the profiles of k during these flights. For all three flights a layer of high

k was observed in a region near the tropopause. It was found that for regions where turbulence was not detected, n trended towards -1, which is believed to be the roll-off of the background sensor noise.

Note that due to the statistical segment length used for averaging, the value of k will only incorporate contributions from wavelengths smaller than the segment length and therefore may not accurately reproduce the actual energy content of the turbulence, as well as being subject to additional scatter introduced by insufficient statistical convergence. An additional metric that can be used to quantify turbulence is the turbulent kinetic energy dissipation rate, ε. As ε tends to scale with the rate of production and magnitude of k, it is often used to quantify the turbulence intensity. This is particularly useful as ε can be determined from small-scale fluctuations and therefore does not require resolution of the largest scales of turbulence while still providing a measure of the relative turbulence intensity over all wavelengths.

As determination of ε using Equation 1 requires measurement of spatial gradients of velocity over distances on the order of the Kolmogorov scale, it is therefore challenging to directly measure in the atmosphere without additional assumptions. Thus, indirect estimates of ε are usually employed. Here, we assume the presence of sufficiently high Reynolds number for the formation of an inertial subrange in the energy spectrum. Under such conditions, the one-dimensional longitudinal wavenumber velocity spectrum in the inertial subrange is expected to follow a scaling such that

$$E_{\ell\ell}(\kappa_\ell) = 0.49\varepsilon^{2/3}\kappa_\ell^{-5/3} \tag{14}$$

(e.g. Saddoughi and Veeravalli, 1994). For the present measurements, this scaling was used to estimate ε by fitting a power-law, i.e. $A\kappa_\ell^n$, to $E_{\ell\ell}$ over the κ_ℓ range corresponding to $\kappa_\ell > 0.1$ and $f < 20$ Hz, thus allowing the estimate

$$\varepsilon = \left(\frac{A}{0.49}\right)^{3/2} \tag{15}$$

to be made for each statistical segment. The low wavenumber bound of $\kappa_\ell = 0.1$ was determined by collectively inspecting the longitudinal velocity spectra and identifying the range of vales which exhibited power law decay.

The corresponding statistic of eddy dissipation rate, $EDR = \varepsilon^{1/3}$, is often used in the aviation industry to quantify turbulence. Qualitatively, the turbulence can be referred to as: steady for $EDR < 0.1$; weak for EDR between 0.1 and 0.3; moderate for EDR between 0.3 and 0.5; strong for EDR between 0.5 and 0.8; and very strong for $EDR > 0.8$. Hence, here we use EDR to describe the turbulent kinetic energy dissipation rate as it allows a qualitative comparison of turbulence intensity to established thresholds.

Profiles of EDR are shown for all three flights in Fig. 11d-f. Note that the approach used is only an approximation of ε as the inertial subrange only rarely follows the -5/3 slope, hence it will provide a non-zero value even if no turbulence is present, and therefore some caution is required when interpreting these EDR profiles beyond being a qualitative indication of the presence of turbulence in the form of localized regions of relatively high EDR. To provide some additional discrimination, as with k, we indicate measurement points when $-1.8 < n < -1.5$ using solid red symbols.

As could be expected, regions of high EDR correspond to regions with high k, although the profiles have different characteristics for these two quantities. For example, the EDR indicates that the aircraft experienced turbulence during Flight 1 (Fig. 11c) near the boundary layer ($z < 3$ km) and within the stratosphere ($z > 18$ km), although the high k region measured at $z = 11$ km does not appear to be as significant according to the EDR metric. For Flights 2 and 3, there was better correspondence between peaks in EDR and regions identified as having an inertial subrange than found for k, with most locations where $-1.8 < n < -1.5$ corresponding to distinct peaks in EDR, with the most active regions appearing near the boundary layer and tropopause. Interestingly, the EDR shows generally enhanced values in the stratosphere, which does not correspond to indications of the presence of a classical inertial subrange with $\kappa_\ell^{-5/3}$.

3.4 Infrasonic Detection of Turbulence

As noted in Section 1, a secondary objective of these experiments was to determine the effectiveness of infrasonic sensing for detecting atmospheric turbulence. Here, we use the amplitude of the acoustic signature quantified using its variance, σ_{IS}^2. Here, σ_{IS}^2 was calculated by integrating energy spectra from the time series of microphone signal for each statistical segment and integrating these spectra over a frequency range of $f < 10$ Hz. This process produces a measure of the amplitude of the infrasonic frequency content for each segment. Some sensitivity of σ_{IS}^2 was observed to both the frequency range and length of statistical segment used for its calculation, with the range used selected due to finding that lower frequency acoustic content better correlated with the EDR values measured with the five-hole-probe when compared to the higher frequency acoustic content, which tended to contain additional signal noise.

Profiles of σ_{IS}^2 are shown for all three flights in Fig. 13. Noticeably, there was a decrease in signal amplitude with altitude measured in all cases. It was found that this decrease closely corresponds to the reduction in local atmospheric pressure, and therefore this decrease is expected to be caused by the increased acoustic attenuation corresponding to the increase in molecular mean free path with altitude. Despite this attenuation, localized increases in σ_{IS}^2 were observed, particularly near the boundary layer, providing an initial confirmation of the presence of infrasonic sound generation by turbulence. Additional localized increases at higher altitudes were also measured, for example during Flight 1 around $z = 4$ km and around $z = 7.5$ km which may correspond to acoustic generation by turbulence in the troposphere, but these altitudes did not directly align with altitudes of increased turbulence in the corresponding profiles of k and EDR. The relationship between these increased peaks in σ_{IS}^2 and measurement location will be examined in more detail in the next section.

3.5 Horizontal Structure of Turbulent Regions

The helical flight path taken by the HiDRON H2 introduces the possibility of expanding the vertical profiles along the circumference of the aircraft's orbit, here represented in the form of azimuthal position, α, of the aircraft relative to the center of the aircraft's orbit. Visualizations in the form of contour maps of selected quantities resulting from this process are presented in Figs. 14, 15 and 16 for Flights 1, 2 and 3 respectively. To smooth and improve the visibility of the contours, a three-point moving average was employed across each three successive statistical segments in time. Also shown on the figures are the (α, z) locations of the statistical segments, colored by their true (non-smoothed) values. When the measurements are examined
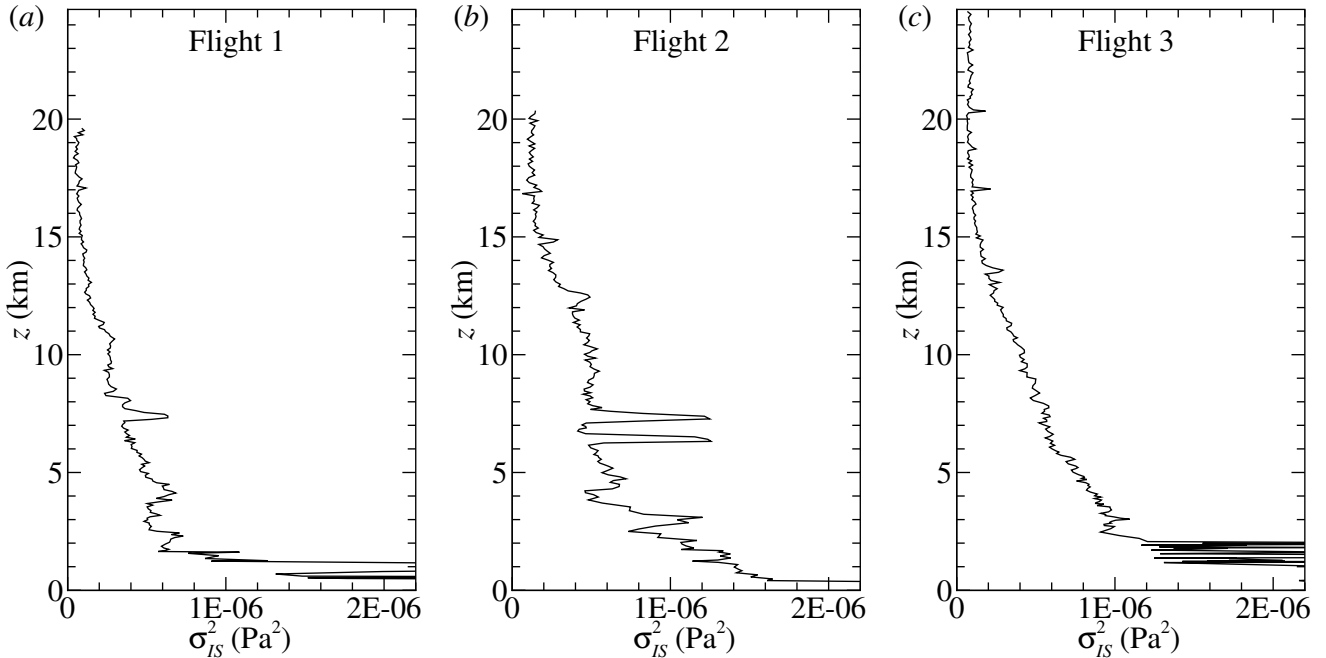
Figure 13. Infrasonic signal amplitude, σ^2_{IS}, profiles measured during (*a*) Flight 1, (*b*) Flight 2, and (*c*) Flight 3.

in this manner, some of the scatter in the vertical profiles was be found to be associated with horizontal heterogeneity in the
590 measured statistics. Due to the variability observed in the S_t, N_t and Ri_t profiles, for this analysis we restrict the visualizations
to S^2_z, N^2_z and Ri_z, although it should be recognized that these values reflect only the influence of the gradients over vertical
distances larger than 2.5 km. We therefore also only examine the behavior of other quantities in terms of relative trends in these
values, rather than specific thresholds.

    Examining Flight 1, the distribution of measured N_z shown in Fig. 14a indicates that the static stability conditions are
595 nearly constant with altitude. Less stratification is evident in the S_z distribution shown in Fig. 14b, although high values of S_z
were evident above and below the jet stream, as could be expected. The resulting Ri_z distribution, shown in Fig. 14c is largely
dominated by the high Ri_z measured at the center of the jet. Note that although the elevated values of Ri_z associated with the jet
stream appears concentrated around $\alpha \approx 0°$, the aircraft trajectory results in sample point spacing whereby the aircraft passes
above or below the high Ri_z layer at the other azimuthal positions. The Ri_z distribution does reflect the lower values which
600 occur where S_z is higher. Higher values of S_z appear to correspond to correspond to elevated values of EDR, as shown in
Fig. 14d, but the velocity spectrum slope n, shown in Fig. 14e indicates that the higher EDR values do not reflect motions with
an established universal equilibrium range, at least at within the resolution of this measurement. However, Fig.14e does show a
region of lower n near the surface at ($\alpha \approx 35°$, $z \approx 4$ km) which extends diagonally away from the surface with positive α and
is possibly connected to a low-n region at ($\alpha \approx -150°$, $z \approx 10$ km). These reduced n contours correlate with elevated EDR
605 values and may be related to turbulence produced in a region of high S_z measured around ($\alpha \approx 45°$, $z \approx 5$ km) suggesting
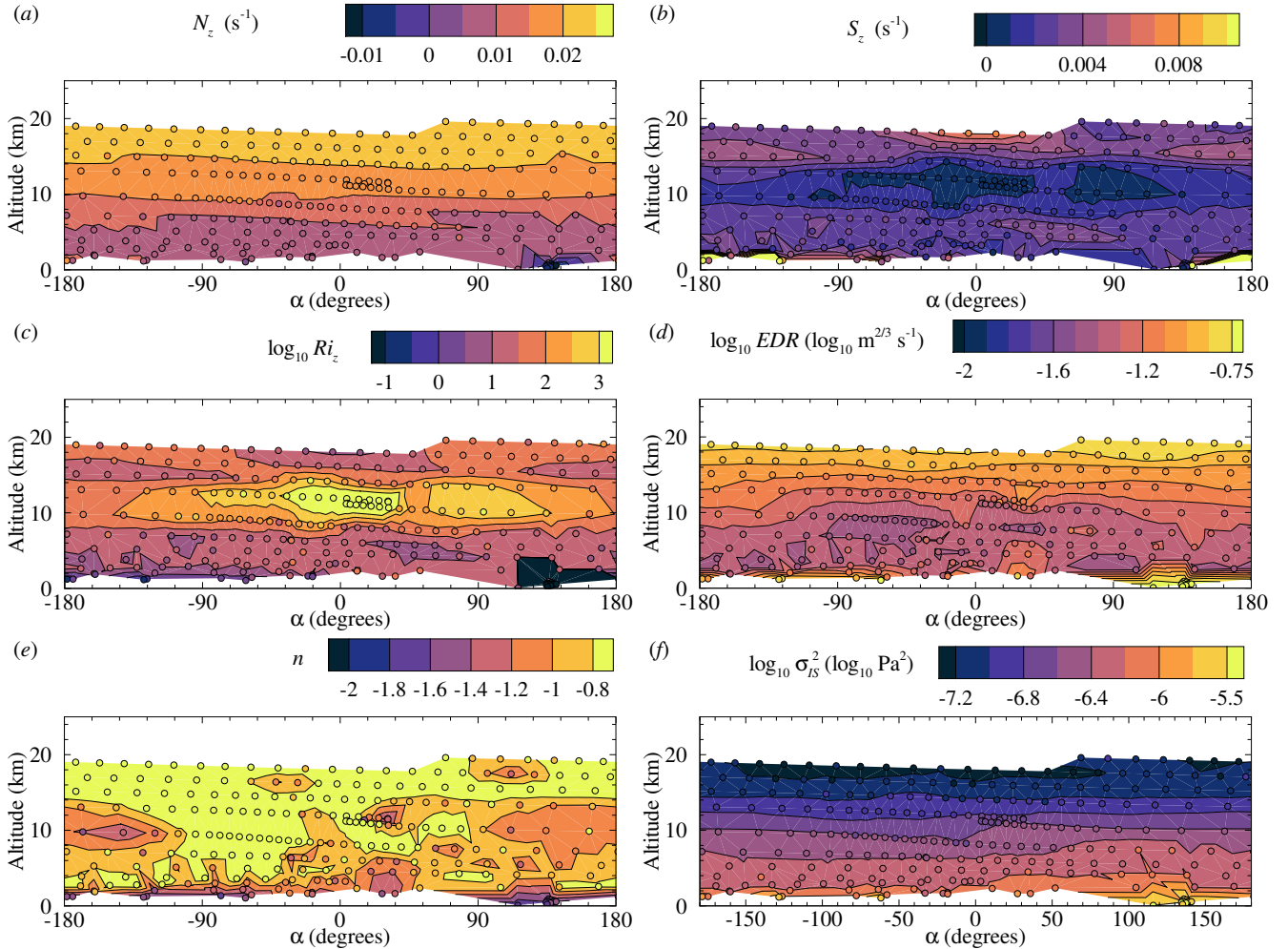
Figure 14. Flight 1 contours of: (*a*) N^2 ; (*b*) S^2; (*c*) Ri; (*d*) EDR; (*e*) n; and (f) σ_{IS}^2. Circles indicate locations of statistical segments at which each quantity calculated.

the higher EDR may be related to shear production in the lower portion of the jet. Conversely, however, a region of high S_z located around ($\alpha \approx -105°, z \approx 5$ km) closely corresponds to a region of reduced EDR and higher n values suggesting that this connection may be fortuitous, although reflecting the spatial heterogeneity in the weak tropospheric turbulence experienced during this flight.

610   The distribution of infrasonic sound amplitude, shown in Fig. 14f, indicates higher infrasonic sound was present in the eastern portion of the flight (positive α) which is consistent with the region of elevated measured EDR values. It should be noted that this elevated σ_{IS}^2 region appears in the form of peaks in the σ_{IS}^2 profiles in Fig. 13a (noticeable at $z = 4$ km, $z = 7.5$ km).
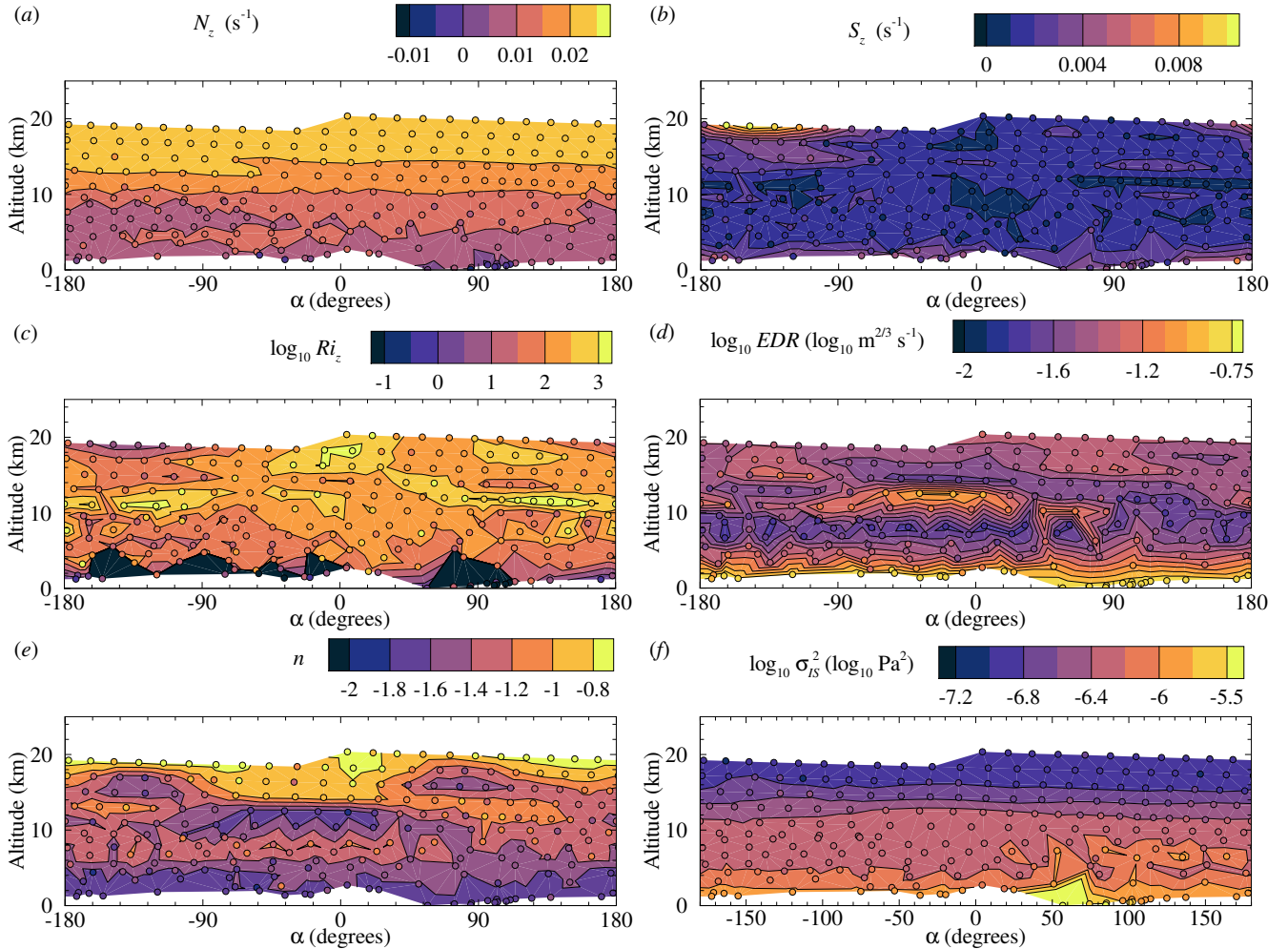
Figure 15. Flight 2 contours of: (a) N^2 ; (b) S^2; (c) Ri; (d) EDR; (e) n; and (f) σ_{IS}^2. Circles indicate locations of statistical segments at which each quantity calculated.

Although the properties measured during Flight 1 were subject to the presence of the jet stream, very different conditions were measured during Flights 2 and 3 which are reflected in the statistical distributions shown in Figs. 15 and 16, respectively.

The organization of structural features measured during Flight 2 are shown in Fig. 15. As with Flight 1, the N^2 distributions appear homogeneous, particularly above the tropopause. However, a region of higher N_z appears near ($\alpha \approx -70°, z \approx 5$ km). The measured S_z shows high shear in the stratosphere at ($\alpha \approx -210°, z \approx 18$ km), with the remaining elevated S_z regions appearing near the boundary layer and in thin layers at $z \approx 15$ km and $z \approx 10$ km. The result is a rather complex Ri_z distribution, as shown in Fig. 15c, which indicates the highest likelihood of turbulence in the regions of highest S_z. The measurements of EDR, shown in Fig. 15d, do indicate the presence of turbulence in these locations, although high EDR values were also measured near ($\alpha \approx 0°, z \approx 10$ km) and ($\alpha \approx 90°, z \approx 17$ km), despite the high Ri_z measured at these locations. The corre-
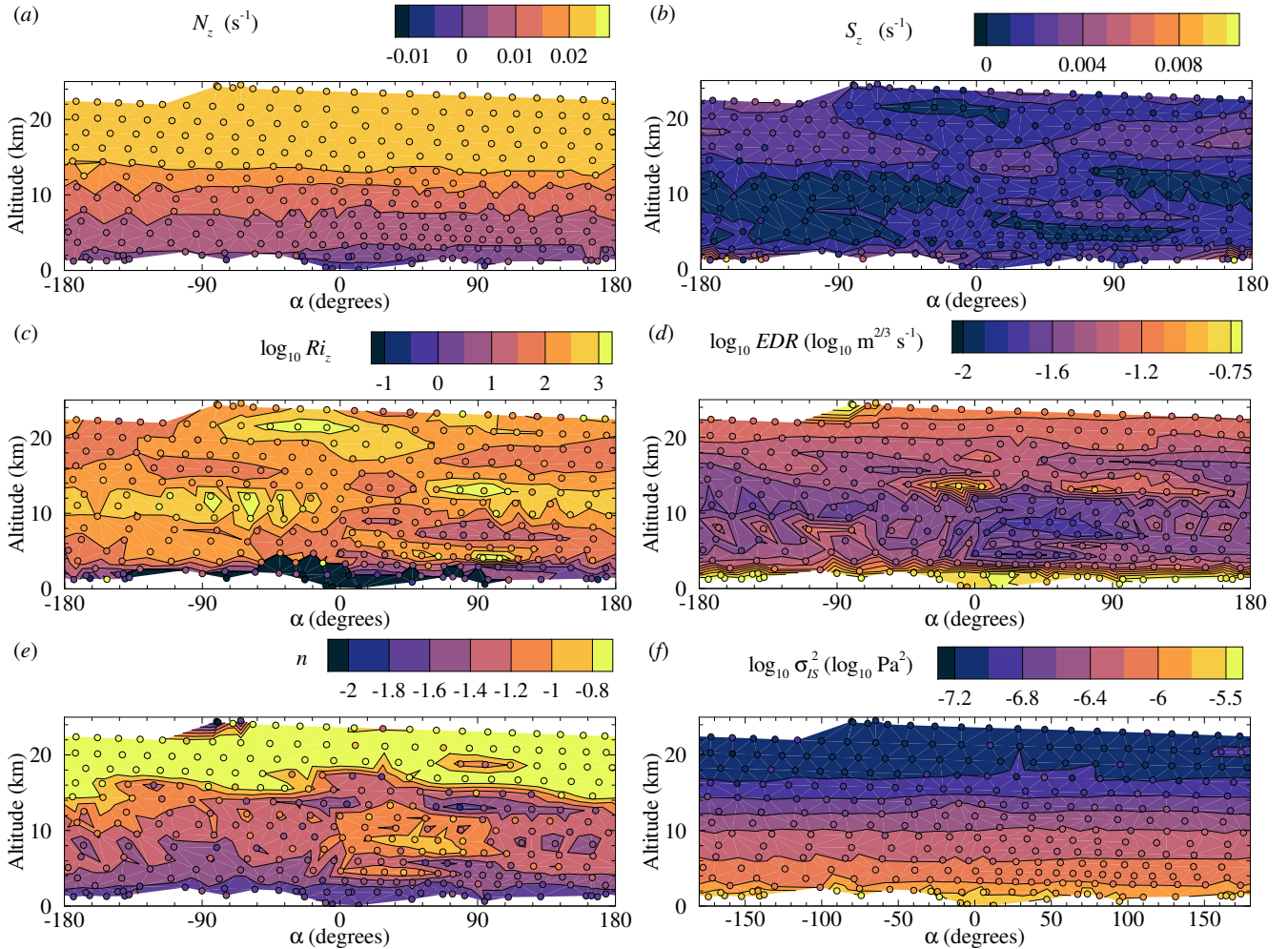
Figure 16. Flight 3 contours of: (*a*) N^2 ; (*b*) S^2; (*c*) Ri; (*d*) EDR; (*e*) n; and (f) σ_{IS}^2. Circles indicate locations of statistical segments at which each quantity calculated.

sponding n values for these regions, as shown in Fig. 15e, are near those expected within the inertial subrange, suggesting that the higher EDR corresponds to the presence of turbulence, even though no clear production mechanism was measured.

625   The distribution of infrasonic sound amplitude for Flight 2, shown in Fig. 15f indicates higher infrasonic sound was also present in the eastern portion of the flight (positive α) in the proximity of the boundary layer, which may be connected with higher measured EDR values in this region. Again, the isolated peaks observed in Fig. 13b near $z = 6.5$ km and $z = 7.5$ km appear to be related spatially. Furthermore, locally elevated σ_{IS}^2 was also measured near ($\alpha \approx -130°, z \approx 17$ km), which may indicate the detection of infrasonic sound waves produced by the wind shear in that region.

630   Broadly similar structure was measured during Flight 3 (Fig. 16) as measured during Flight 2. With a nearly uniform N_z distribution (Fig. 16a) and stratified S_z distribution (Fig. 16b) leading to a similar Ri_z distribution (Fig. 16c) to that measured

during Flight 2. Interestingly, a region of high S_z near ($\alpha \approx 90°, z \approx 8$ km) corresponds to a region of locally reduced EDR and higher n (Fig. 16e). Instead, high EDR was measured at ($\alpha \approx 0°, z \approx 14$ km) and ($\alpha \approx 90°, z \approx 14$ km) where locally high Ri_z values were observed. The σ_{IS}^2 distributions shown in Fig. 16f are largely homogeneous in the horizontal plane, with the highest amplitudes measured near the boundary layer.

4 Summary and Conclusions

This work demonstrates how a sUAS in the form of a balloon-launched glider can be used to conduct detailed analysis of the statistical structure of atmospheric turbulence over a range of altitudes typically interrogated using weather balloons. In the measurements described here, the particular aircraft was equipped with a five-hole-probe for measuring the three-component wind vector, and a pressure, temperature and humidity sensing system integrated into the aircraft.

These instruments allowed the calculation of vertical profiles of T, RH, U and γ which compared favorably with publicly-available radiosonde data from the National Weather Service. In addition, the slow, spiralling descent allowed for the calculation of spatially-averaged statistics such as k and ε with high vertical resolution. The resulting vertical profiles suggest that isolated regions of turbulence were present in all three flights, although enhanced values of ε in the stratosphere, represented using EDR, were produced despite the kinetic energy content not containing the characteristic roll-off expected for inertial range turbulence. Furthermore, a comparison of the gradient Richardson number and and the EDR measured at the same location suggested that there was only a general connection between the two parameters, with multiple measurements of turbulent values of EDR made in regions identified as being stable through the corresponding values of N^2, with high Ri measured at those locations. This is likely due to the ambiguity in Richardson number calculation introduced by the spiral flight path into the vertical gradient calculation. To resolve this ambiguity, the helical flight path could be conducted over a reduced radius, resulting in a reduced vertical separation between successive orbits.

The helical trajectory taken by the glider during its descent did introduce the possibility to produce depictions of the horizontal heterogeneity of multiple parameters measured during the descent making it possible to visualize the structure of the motions measured along the flight path. These visualizations were found to show that many of the features which appear in isolation on the vertical profiles were actually produced by the aircraft passing through the same structure more than once. Using these visualizations also allowed some regions of increased EDR to be related to locally high regions of S_z, although other locations of high EDR occurred where N^2 was high and S^2 low, and regions of high S^2 corresponding to regions of low EDR. These discrepancies may be due to the method of calculation of the vertical gradients, as noted above, which were calculated using measurement points across neighboring orbits (rather than measurement points along the same orbit). This approach meant that the smallest vertical scale which could be resolved by these gradients was on the order of 2.5 km, whereas a smaller orbit radius and statistical segment lengths would have allowed higher resolution of the vertical gradients.

Despite this ambiguity, these initial flights suggest that the sUAS measurements suggest the potential exists to make connections between regions of increased turbulence and their generating mechanisms and it would be difficult to draw the same associations using balloon-based measurements. From a purely statistical viewpoint, the ability of the aircraft to orbit around

665 a fixed geographical point, rather than travelling with the wind, eases horizontal localization of the measurements. In addition, the flight pattern allows for increased statistical convergence due to the larger volume of air sampled over a particular altitude range. To highlight this point, for a 1000 m of altitude change, during the experiments described here, the orbit of the sUAS allowed it to sample the atmosphere for a distance of approximately 15,000 m, whereas comparable in-situ measurements by a balloon would have sampled only the 1000 m column along its ascent path.

670   Finally, a secondary objective of this study was to assess the feasibility of implementing an infrasonic microphone on a sUAS for detecting clear air turbulence. The results of this study suggest that the infrasonic microphone can detect turbulent features, particularly near the stronger boundary layer turbulence. However, for the weaker tropospheric and stratospheric turbulence experienced during these flights, it was difficult to conclusively link regions of higher infrasonic noise detection to higher turbulence once out of the boundary layer. These difficulties were contributed to by the remote-sensing nature of

675 this instrument, its altitude sensitivity, and the broad-band nature of turbulent sound generation, which make it challenging to discriminate discrete turbulent events. Future work will seek to improve the resolution of the data acquisition system, as well as to deploy these microphones in arrays, which will better enable the discrimination of discrete noise-generating events from the ambient background noise.

Data availability. Data from these flights are available from the corresponding author on request.

680 *Video supplement.* A video compilation of aircraft preparation, flight and recovery is publicly available at https://vimeo.com/568101900

Author contributions. S.B., G.P., N.C. planned the experiment which was realized by S.B., R.N., G.P. and A.S.. Data analysis was conducted by A.H. and S.B. who also prepared the initial draft of the manuscript with input from the remaining authors.

Competing interests. The authors declare no competing interests are present.

Acknowledgements. Financial support for this work was provided by NASA under the Flight Opportunities Program through award number

685 80NSSC20K0102 with Paul A. De León as the NASA Technical Officer. The authors would also like to dedicate this work to Dr. Qamar Shams who worked at NASA Langley Research Center and graciously assisted with the implementation and the loan of the infrasonic microphone from NASA.

References

Abarbanel, H. D. I., Holm, D. D., Marsden, J. E., and Ratiu, T.: Richardson Number Criterion for the Nonlinear Stability of Three-Dimensional Stratified Flow, Phys. Rev. Lett., 52, 2352–2355, https://doi.org/10.1103/PhysRevLett.52.2352, 1984.

Al-Ghussain, L. and Bailey, S. C. C.: An approach to minimize aircraft motion bias in multi-hole probe wind measurements made by small unmanned aerial systems, Atmospheric Measurement Techniques, 14, 173–184, https://doi.org/10.5194/amt-14-173-2021, 2021.

Al-Ghussain, L. and Bailey, S. C. C.: Uncrewed Aircraft System Measurements of Atmospheric Surface-Layer Structure During Morning Transition, Boundary-Layer Meteorology, 185, 229–258, https://doi.org/10.1007/s10546-022-00729-2, 2022.

Alisse, J.-R., Haynes, P. H., Vanneste, J., and Sidi, C.: Quantification of stratospheric mixing from turbulence microstructure measurements, Geophysical Research Letters, 27, 2621–2624, https://doi.org/https://doi.org/10.1029/2000GL011386, 2000.

Bailey, S. C. C., Canter, C. A., Sama, M. P., Houston, A. L., and Smith, S. W.: Unmanned aerial vehicles reveal the impact of a total solar eclipse on the atmospheric surface layer, Proceedings of the Royal Society A: Mathematical, Physical and Engineering Sciences, 475, 20190 212, https://doi.org/10.1098/rspa.2019.0212, 2019.

Bailey, S. C. C., Sama, M. P., Canter, C. A., Pampolini, L. F., Lippay, Z. S., Schuyler, T. J., Hamilton, J. D., MacPhee, S. B., Rowe, I. S., Sanders, C. D., Smith, V. G., Vezzi, C. N., Wight, H. M., Hoagg, J. B., Guzman, M. I., and Smith, S. W.: University of Kentucky measurements of wind, temperature, pressure and humidity in support of LAPSE-RATE using multisite fixed-wing and rotorcraft unmanned aerial systems, Earth System Science Data, 12, 1759–1773, https://doi.org/10.5194/essd-12-1759-2020, 2020.

Balsley, B. B., Lawrence, D. A., Woodman, R. F., and Fritts, D. C.: Fine-scale characteristics of temperature, wind, and turbulence in the lower atmosphere (0–1,300 m) over the south Peruvian coast, Boundary-Layer Meteorology, 147, 165–178, 2013.

Balsley, B. B., Lawrence, D. A., Fritts, D. C., Wang, L., Wan, K., and Werne, J.: Fine Structure, Instabilities, and Turbulence in the Lower Atmosphere: High-Resolution In Situ Slant-Path Measurements with the DataHawk UAV and Comparisons with Numerical Modeling, Journal of Atmospheric and Oceanic Technology, 35, 619–642, https://doi.org/10.1175/JTECH-D-16-0037.1, 2018.

Barat, J. and Bertin, F.: Simultaneous Measurements of Temperature and Velocity Fluctuations Within Clear Air Turbulence Layers. Analysis of the Estimate of Dissipation Rate by Remote Sensing Techniques, Journal of the Atmospheric Sciences, 41, 1613–1619, https://doi.org/10.1175/1520-0469(1984)041<1613:SMOTAV>2.0.CO;2, 1984.

Barbieri, L., Kral, S. T., Bailey, S. C. C., Frazier, A. E., Jacob, J. D., Reuder, J., Brus, D., Chilson, P. B., Crick, C., Detweiler, C., Doddi, A., Elston, J., Foroutan, H., González-Rocha, J., Greene, B. R., Guzman, M. I., Houston, A. L., Islam, A., Kemppinen, O., Lawrence, D., Pillar-Little, E. A., Ross, S. D., Sama, M. P., Schmale, D. G., Schuyler, T. J., Shankar, A., Smith, S. W., Waugh, S., Dixon, C., Borenstein, S., and de Boer, G.: Intercomparison of Small Unmanned Aircraft System (sUAS) Measurements for Atmospheric Science during the LAPSE-RATE Campaign, Sensors, 19, https://doi.org/10.3390/s19092179, 2019.

Bärfuss, K., Pätzold, F., Altstädter, B., Kathe, E., Nowak, S., Bretschneider, L., Bestmann, U., and Lampert, A.: New setup of the UAS ALADINA for measuring boundary layer properties, atmospheric particles and solar radiation, Atmosphere, 9, https://doi.org/10.3390/atmos9010028, 2018.

Bertin, F., Barat, J., and Wilson, R.: Energy dissipation rates, eddy diffusivity, and the Prandtl number: An in situ experimental approach and its consequences on radar estimate of turbulent parameters, Radio Science, 32, 791–804, https://doi.org/https://doi.org/10.1029/96RS03691, 1997.

Bohn, D. and Simon, H.: Mehrparametrige Approximation der Eichräume und Eichflächen von Unterschall-bzw. Überschall-5-Loch-Sonden, tm-Technisches Messen, 468, 81–89, 1975.

725 Bowman, D. C. and Lees, J. M.: Infrasound in the middle stratosphere measured with a free-flying acoustic array, Geophysical Research Letters, 42, https://doi.org/10.1002/2015GL066570, 2015.

Calmer, R., Roberts, G. C., Preissler, J., Sanchez, K. J., Derrien, S., and O'Dowd, C.: Vertical wind velocity measurements using a five-hole probe with remotely piloted aircraft to study aerosol–cloud interactions, Atmospheric Measurement Techniques, 11, 2583–2599, https://doi.org/10.5194/amt-11-2583-2018, 2018.

730 Chunchuzov, I. P., Kulichkov, S. N., Popov, O. E., and Perepelkin, V. G.: Infrasound generation by meteorological fronts and its propagation in the atmosphere, https://doi.org/10.1175/jas-d-20-0253.1, 2021.

Cunningham, P. and Keyser, D.: SYNOPTIC METEOROLOGY | Jet Streaks, in: Encyclopedia of Atmospheric Sciences (Second Edition), edited by North, G. R., Pyle, J., and Zhang, F., pp. 359–369, Academic Press, Oxford, second edition edn., https://doi.org/https://doi.org/10.1016/B978-0-12-382225-3.00187-0, 2015.

735 Cuxart, J., Tatrai, D., Weidinger, T., Kircsi, A., Józsa, J., and Kiss, M.: Infrasound as a Detector of Local and Remote Turbulence, Boundary-Layer Meteorology, 159, 185–192, https://doi.org/10.1007/s10546-015-0100-2, 2015.

D'Oliveira, F., Melo, F., and Devezas, T.: High-Altitude Platforms - Present Situation and Technology Trends, Journal of Aerospace Technology and Management, 8, 249–262, https://doi.org/10.5028/jatm.v8i3.699, 2016.

Egger, J., Bajrachaya, S., Heingrich, R., Kolb, P., Lammlein, S., Mech, M., Reuder, J., Schäper, W., Shakya, P., Shween, J., and H., W.:
740 Diurnal Winds in the Himalayan Kali Gandaki Valley. Part III: Remotely Piloted Aircraft Soundings, Mon. Wea. Rev., 130, 2042–2058, 2002.

Ehrenberger, L. J.: Stratospheric Turbulence Measurements and Models for Aerospace Plane Design, Tech. Rep. TM-104262, NASA, 1992.

Enlich, R. and Mancuso, R.: The Turbulence Climatology of the United States between 20,000 and 45,000 Feet Estimated from Aircraft Reports and Meteorological Data, Tech. rep., Stanford Research Institute, https://apps.dtic.mil/sti/pdfs/AD0672988.pdf, 1968.

745 Fukao, S., Yamanaka, M. D., Ao, N., Hocking, W. K., Sato, T., Yamamoto, M., Nakamura, T., Tsuda, T., and Kato, S.: Seasonal variability of vertical eddy diffusivity in the middle atmosphere: 1. Three-year observations by the middle and upper atmosphere radar, Journal of Geophysical Research: Atmospheres, 99, 18 973–18 987, https://doi.org/https://doi.org/10.1029/94JD00911, 1994.

Galperin, B., Sukoriansky, S., and Anderson, P. S.: On the critical Richardson number in stably stratified turbulence, Atmospheric Science Letters, 8, 65–69, https://doi.org/https://doi.org/10.1002/asl.153, 2007.

750 Gavrilov, N. M., Luce, H., Crochet, M., Dalaudier, F., and Fukao, S.: Turbulence parameter estimations from high-resolution balloon temperature measurements of the MUTSI-2000 campaign, Annales Geophysicae, 23, 2401–2413, https://doi.org/10.5194/angeo-23-2401-2005, 2005.

Gonzalo, J., Lopez, D., Domínguez Fernández, D., García, A., and Escapa, A.: On the capabilities and limitations of high altitude pseudo-satellites, Progress in Aerospace Sciences, https://doi.org/10.1016/j.paerosci.2018.03.006, 2018.

755 Haack, A., Gerding, M., and Lübken, F.-J.: Characteristics of stratospheric turbulent layers measured by LITOS and their relation to the Richardson number, Journal of Geophysical Research: Atmospheres, 119, 10,605–10,618, https://doi.org/10.1002/2013JD021008, 2014.

Hamilton, J., de Boer, G., Doddi, A., and Lawrence, D. A.: The DataHawk2 uncrewed aircraft system for atmospheric research, Atmospheric Measurement Techniques, 15, 6789–6806, https://doi.org/10.5194/amt-15-6789-2022, 2022.

Hasan, Y., Roeser, M., Hepperle, M., Niemann, S., Voß, A., Handojo, V., and Weiser, C.: Flight mechanical analysis of a solar-powered
760 high-altitude platform, CEAS Aeronautical Journal, 14, https://doi.org/10.1007/s13272-022-00621-2, 2022.

Hobbs, S., Dyer, D., Courault, D., Olioso, A., Lagouarde, J.-P., Kerr, Y., McAnneney, J., and Bonnefond, J.: Surface layer profiles of air temperature and humidity measured from unmanned aircraft, Agronomie, 22, 635–640, https://doi.org/10.1051/agro:2002050, 2002.

Huang, R., Sun, H., Wu, C., Wang, C., and Lu, B.: Estimating Eddy Dissipation Rate with QAR Flight Big Data, Applied Sciences, 9, 5192, https://doi.org/10.3390/app9235192, 2019.

765 International Met Systems: iMet-XF UAV Sensor Description, https://www.intermetsystems.com/products/imet-xf-uav-sensor/, accessed: 2023-08-04.

Jacob, J. D., Chilson, P. B., Houston, A. L., and Smith, S. W.: Considerations for Atmospheric Measurements with Small Unmanned Aircraft Systems, Atmosphere, 9, https://doi.org/10.3390/atmos9070252, 2018.

Kantha, L., Lawrence, D., Luce, H., Hashiguchi, H., Tsuda, T., Wilson, R., Mixa, T., and Yabuki, M.: Shigaraki UAV-Radar Ex-
770 periment (ShUREX): overview of the campaign with some preliminary results, Progress in Earth and Planetary Science, 4, https://doi.org/10.1186/s40645-017-0133-x, 2017.

Kim, S.-H., Chun, H.-Y., Kim, J.-H., Sharman, R. D., and Strahan, M.: Retrieval of eddy dissipation rate from derived equivalent vertical gust included in Aircraft Meteorological Data Relay (AMDAR), Atmospheric Measurement Techniques, 13, 1373–1385, https://doi.org/10.5194/amt-13-1373-2020, 2020.

775 Ko, H.-C., Chun, H.-Y., Wilson, R., and Geller, M. A.: Characteristics of Atmospheric Turbulence Retrieved From High Vertical-Resolution Radiosonde Data in the United States, Journal of Geophysical Research: Atmospheres, 124, 7553–7579, https://doi.org/https://doi.org/10.1029/2019JD030287, 2019.

Kolmogorov, A. N.: The local structure of turbulence in incompressible viscous fluid for very large Reynolds numbers, Dokl. Akad. Nauk SSSR, 30, 301–305, 1941.

780 Lawrence, D. A. and Balsley, B. B.: High-Resolution Atmospheric Sensing of Multiple Atmospheric Variables Using the DataHawk Small Airborne Measurement System, Journal of Atmospheric and Oceanic Technology, 30, 2352–2366, https://doi.org/10.1175/JTECH-D-12-00089.1, 2013.

Lenschow, D.: The measurement of air velocity and temperature using the NCAR Buffalo aircraft measuring system, National Center for Atmospheric Research, 1972.

785 Luce, H., Kantha, L., Hashiguchi, H., Doddi, A., Lawrence, D., and Yabuki, M.: On the Relationship between the TKE Dissipation Rate and the Temperature Structure Function Parameter in the Convective Boundary Layer, Journal of the Atmospheric Sciences, 77, 2311–2326, https://doi.org/https://doi.org/10.1175/JAS-D-19-0274.1, 2020.

NASA: NASA Worldview Snapshots, https://wvs.earthdata.nasa.gov, accessed: 2023-07-28.

Rautenberg, A., Graf, M. S., Wildmann, N., Platis, A., and Bange, J.: Reviewing wind measurement approaches for fixed-wing unmanned
790 aircraft, Atmosphere, 9, 1–24, https://doi.org/10.3390/atmos9110422, 2018.

Reuder, J., Jonassen, M. O., and Ólafsson, H.: The Small Unmanned Meteorological Observer SUMO: Recent developments and applications of a micro-UAS for atmospheric boundary layer research, Acta Geophysica, 60, 1454–1473, https://doi.org/10.2478/s11600-012-0042-8, 2012.

Saddoughi, S. G. and Veeravalli, S. V.: Local isotropy in turbulent boundary layers at high Reynolds number, J. Fluid Mech., 268, 333–372,
795 1994.

Sato, T. and Woodman, R. F.: Fine Altitude Resolution Observations of Stratospheric Turbulent Layers by the Arecibo 430 MHz Radar, Journal of the Atmospheric Sciences, 39, 2546–2552, https://doi.org/10.1175/1520-0469(1982)039<2546:FAROOS>2.0.CO;2, 1982.

Shams, Q. A., Zuckerwar, A. J., Burkett, C. G., Weistroffer, G. R., and Hugo, D. R.: Experimental investigation into infrasonic emissions from atmospheric turbulence, The Journal of the Acoustical Society of America, 133, 1269–1280, https://doi.org/10.1121/1.4776180,
800 2013.

Sharman, R. D., Cornman, L. B., Meymaris, G., Pearson, J., and Farrar, T.: Description and Derived Climatologies of Automated In Situ Eddy-Dissipation-Rate Reports of Atmospheric Turbulence, Journal of Applied Meteorology and Climatology, 53, 1416–1432, https://doi.org/10.1175/JAMC-D-13-0329.1, 2014.

Söder, J., Gerding, M., Schneider, A., Dörnbrack, A., Wilms, H., Wagner, J., and Lübken, F.-J.: Evaluation of wake influence on high-resolution balloon-sonde measurements, Atmospheric Measurement Techniques, 12, 4191–4210, https://doi.org/10.5194/amt-12-4191-2019, 2019.

Söder, J., Zülicke, C., Gerding, M., and Lübken, F.-J.: High-Resolution Observations of Turbulence Distributions Across Tropopause Folds, Journal of Geophysical Research: Atmospheres, 126, https://doi.org/10.1029/2020JD033857, 2021.

Treaster, A. L. and Yocum, A. M.: The calibration and application of five-hole probes, Tech. rep., DTIC Document, 1978.

van den Kroonenberg, A., Martin, T., Buschmann, M., Bange, J., and Vörsmann, P.: Measuring the Wind Vector Using the Autonomous Mini Aerial Vehicle M^{2}AV, J. Atmos. Oceanic Technol., 25, 1969–1982, 2008.

Van den Kroonenberg, A., Martin, T., Buschmann, M., Bange, J., and Vörsmann, P.: Measuring the wind vector using the autonomous mini aerial vehicle M2AV, Journal of Atmospheric and Oceanic Technology, 25, 1969–1982, 2008.

Wescott, J., SCIENCE, M. U. A. A. I. O., and TECHNOLOGY.: Acoustic Detection of High - Altitude Turbulence, Defense Technical Information Center, https://books.google.com/books?id=pkBFGwAACAAJ, 1964.

Whitaker, R. W. and Norris, D. E.: Infrasound Propagation, https://doi.org/10.1007/978-0-387-30441-0_82, 2008.

Wildmann, N., Hofsäß, M., Weimer, F., Joos, A., and Bange, J.: MASC–a small Remotely Piloted Aircraft (RPA) for wind energy research, Advances in Science and Research, 11, 55–61, 2014.

Witte, B. M., Singler, R. F., and Bailey, S. C.: Development of an Unmanned Aerial Vehicle for the Measurement of Turbulence in the Atmospheric Boundary Layer, Atmosphere, 8, 195, 2017.

Appendix A: Upper Air Maps and Satellite Imagery
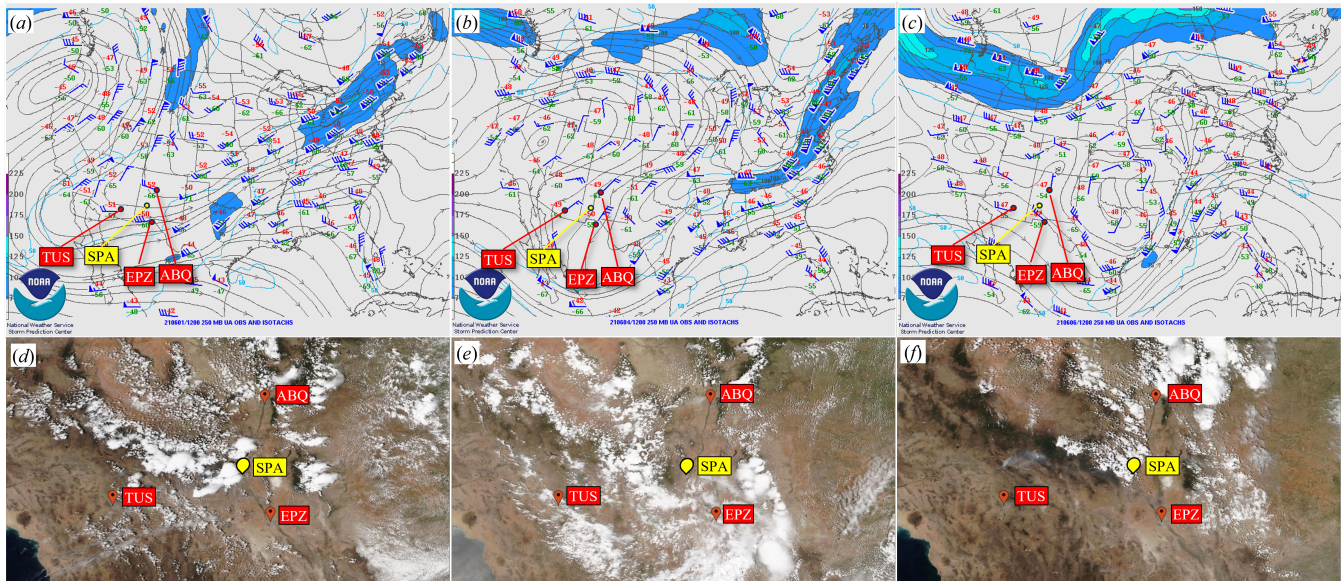
Figure A1. NOAA Jet stream maps at 250 mb (10.366 km) for (a) Flight 1, (b) Flight 2, (c) Flight 3 and satellite images of cloud cover (NASA) for (d) Flight 1, (e) Flight 2, (f) Flight 3. Red pins indicate NWS sounding sites and yellow pin indicates measurement location at SpacePort America (SPA).